Universidade de Aveiro
Ano 2022/2023

Francisco Henriques Duarte

Valorização de um resíduo industrial rico em ferro por eletrodeposição para a produção de aço

Universidade de Aveiro
Ano 2022/2023

Francisco Henriques Duarte

Valorization of an industrial iron-rich residue by electroreduction for steel production

Dissertação apresentada à Universidade de Aveiro para cumprimento dos requisitos necessários à obtenção do grau de Mestre em Engenharia de Materiais, realizada sob a orientação científica do Doutor Aleksey D. Lisenkov e da Doutora Daniela Vanessa Rosendo Lopes, do Departamento de Engenharia de Materiais e Cerâmica da Universidade de Aveiro.

o júri

presidente

Prof. Doutor João António Labrincha Batista
Professor Associado do Departamento de Engenharia de Materiais e Cerâmica da Universidade de Aveiro

vogais

Prof. Doutor Duncan Paul Fagg
Investigador Principal associado do Departamento de Engenharia Mecânica da Universidade de Aveiro

Doutora Daniela Vanessa Rosendo Lopes
Investigadora Doutorada do Departamento de Engenharia de Materiais e Cerâmica, CICECO da Universidade de Aveiro

agradecimentos

Com a realização da tese de mestrado, tenho o dever e o prazer de agradecer a todos os que me ajudaram ao longo do percurso.

Primeiramente tenho de agradecer aos meus incríveis orientadores, Doutor Aleksey D. Lisenkov e Doutora Daniela Vanessa Rosendo Lopes, pelo constante acompanhamento e apoio ao longo desta longa aventura. Atribulada, com vários percalços pelo caminho superados com a ajuda deles, sempre prontos a reagir às circunstâncias. Aprendi bastante a nível científico, e também como é o dia-dia da vida de um cientista/investigador.

Aos docentes presentes no laboratório “Lab of Solid State Ionics and Energy Conversion”, pela sua prontidão em me auxiliar e pela animação. Com uma especial menção à investigadora Isabel Antunes por me facultar a sua centrifuga que no início do trabalho prático foi essencial para obter as primeiras gramas de β-FeOOH de modo a entender qual o melhor método de síntese para uma β-FeOOH mais pura e cristalina. Também, à Doutora Paula Celeste da Silva Ferreira pela disponibilidade da centrifuga pertencente ao CICECO, para começar a produzir β-FeOOH em maiores quantidades.

Agradecimento ao projeto europeu SIDERWIN pela oportunidade de investigar esta tecnologia embrionária cada vez mais relevante com o passar dos anos (referência – SIDERWIN-DLV768788-Horizon 2020/SPIRE10).

Por fim, mas não tão menos importante, agradecer aos meus pais pela ajuda emocional e financeira para a conclusão do curso.

palavras-chave Akaganeite, eletrólise alcalina, eletroredução, ferro, redução, resíduo

resumo

Perante o desafio de atenuar as consequências das alterações climáticas, é de extrema importância o desenvolvimento de processos energeticamente eficientes e com baixas emissões de CO_2 para a atmosfera, na produção de ferro e aço. Ao longo dos anos, a redução eletroquímica direta tem vindo a receber cada vez mais atenção como processo que realiza eficientemente reduções in-situ em meio alcalino, com produção de subprodutos, como o hidrogénio e oxigénio. Esta tecnologia integra as energias renováveis, reduzindo em 87% as emissões de CO_2. Neste âmbito, o presente trabalho teve como objetivo a produção de ferro com recurso à inovadora redução eletroquímica de suspensões alcalinas de akaganeite (β-FeOOH) a baixas temperaturas, com o intuito de estudar as perspetivas de usar um resíduo metalúrgico, como fonte de óxido de ferro. O resíduo estudado para este feito é proveniente da produção de níquel por via eletrólitca e com composição baseada em β-FeOOH. De modo a comparar os resultados obtidos com uma composição sintética de óxidos de ferro já estudada na literatura, escolheu-se a hematite (Fe_2O_3) como referência. A deposição de ferro foi efetuada na condição galvanostática e potenciostática durante 16 horas. Esta última, permitiu a otimização na composição microestrutural do ferro. As composições sintéticas de β-FeOOH e Fe_2O_3, bem como o resíduo industrial, foram adicionados a eletrólitos de 10 M de NaOH a 90 ºC e a 18 M de NaOH para as temperaturas de 105, 120 e 130 ºC. As condições experimentais selecionadas, possibilitaram deposições de ferro eficientes sem uma evolução significativa de hidrogénio, permitindo um aumento na eficiência em comparação com a deposição de sais de ferro dissolvidos ou suspensões ácidas convencionais. Os mecanismos de redução eletroquímica foram estudados através da voltametria cíclica. É possível obter depósitos de ferro através da redução da composição sintética de β-FeOOH. No entanto, devido ao aumento da viscosidade do eletrólito ao longo da deposição, a eficiência Faradaica foi, de apenas ~4%. Apesar da pouca reprodutibilidade obtida a partir de suspensões sintéticas, o uso do resíduo facilitou eficientemente a eletrodeposição de ferro, apresentando resultados de eficiência semelhantes ao das suspensões de Fe_2O_3. A deposição galvanostática a 90 ºC atingiu 59% de eficiência Faradaica, uma diferença de apenas ~2% da eficiência obtida na suspensão de Fe_2O_3 nas mesmas condições experimentais. A eficiência diminuiu, de forma geral com o aumento da temperatura de deposição em ambos os casos da utilização do resíduo e Fe_2O_3 a 18 M de NaOH. Por fim, a deposição potenciostática do resíduo apresentou eficiências Faradaicas elevadas, 91% a -1.075 V até os 83% a -1.15 V. Estudos combinados de XRD/SEM/EDS, comprovaram a presença de cristais de ferro em todas as deposições. Conclui-se que é possível produzir ferro através de suspensões sintéticas (β-FeOOH e Fe_2O_3), como também de resíduos industriais à base de β-FeOOH. O resíduo industrial provou ser uma matéria-prima viável para a produção eletrolítica de ferro.

keywords Alkaline electrolysis, akaganeite, electroreduction, reduction, residue

abstract

The development of energy-efficient, carbon-free, and environmentally friendly routes to produce iron and steel is critical for the climate change mitigation. Electrochemical reduction of iron oxides has been gaining attention as a process allowing in-situ reduction, under strong alkaline media with hydrogen and oxygen as by-products. This technology also considers the integration of renewable energies and reduces 87% of CO_2 emissions. In this scope, the present work consists the study of novel electrochemical reduction of akaganeite (β-FeOOH) particle suspensions into iron, under a strongly alkaline solution at low temperature, to study the prospects of using a metallurgical residue as an iron oxide source. The by-product of nickel manufacture is also studied in the frame of this work. Moreover, it was studied other synthetic oxide composition, such as hematite (Fe_2O_3) for comparison purposes. The iron deposition was performed in both galvanostatic and potentiostatic conditions for 16 hours. This allowed the microstructural iron optimization. The synthetic β-FeOOH and Fe_2O_3, as well as the industrial residue suspensions were added to 10 M of NaOH electrolyte at low temperatures of 90 ºC and 18 M of NaOH at 105, 120 and 130 ºC. The selected experimental conditions ensure efficient deposition of iron without significant evolution of hydrogen, allowing an efficiency increase in comparison to the deposition from dissolved iron salts or conventional acidic suspensions. Cyclic-voltammetry was used to study the electrochemical mechanism of reduction. Iron depositions from the β-FeOOH synthetic composition were accessed yet due to the high viscosity of the electrolyte, very low Faradaic efficiencies were achieved, reaching ~4%. Despite the low reproducibility of the synthetic β-FeOOH, promising results were obtained with the residue (β-FeOOH based composition), being not significantly less efficient when compared with the Fe_2O_3 suspensions. The galvanostatic deposition at 90 ºC reached 59% Faradaic efficiency, mere ~2% above the Faradaic Efficiency of Fe_2O_3 suspensions in the same conditions. At higher temperatures with 18 M of NaOH generally, the Faradaic efficiency decrease as the temperature increases, such as for the Fe_2O_3 suspensions, only to reach higher Faradaic efficiencies. The potentiostatic deposition at -1.075 V reached a maximum of 91% of Faradaic Efficiency and 83% at -1.15 V. Combined studies of XRD/SEM/EDS proved the presence of Fe crystals in all electrochemical tests. Certain differences in iron microstructure were found. It is shown that Fe production can be achieved in both synthetic β-FeOOH and Fe_2O_3 as well for the industrial residue. The used industrial residue proved to be a suitable alternative feedstock for the electrolytic production.

Index

List of figures

List of tables

List of abbreviations

	Name	**Unit**
BF-BOF	Blast Furnace-Basic Oxygen Furnace	-
CE	Counter Electrode	-
DRI-EAF	Direct Reduced Iron Electric Arc Furnace	-
EDS	Energy Dispersive Spectrometer	-
HER	Hydrogen Evolution Reaction	-
IERO	Iron production by Electrochemical Reduction of its Oxide	-
NR	Nikkelverk Residue	-
PIDS	Polarization Intensity Differential Scattering	-
PM	Dust/Particulate Matter	-
PTFE	Polytetrafluoroethylene	-
REE	Rare Earth Element	-
SEM	Scanning Electron Microscope	-
SHE	Standard Hydrogen Electrode	-
ULCOS	Ultralow CO_2 in Steelmaking	-
UNFCCC	United Nations Framework Convention on Climate Change	-
WE	Working Electrode	-
XRD	X-Ray Diffraction	-
XRF	X-ray fluorescence spectroscopy	-

List of symbols

a_{Ox}	Activities of Oxidized Species	-
a_{Red}	Activities of Reduced Species	-
F	Faradaic Constant	$C.mol^{-1}$
ΔG	Gibbs Free Energy	$kJ.mol^{-1}$
G	Gibbs	$kJ.mol^{-1}$
I	Current	A
M	Molar mass	$g.mol^{-1}$
R	Molar gas constant	$J.K^{-1}.mol^{-1}$
T	Temperature	K
t	Time	s
V	Potential	V
z	Number of electrons	-

1. Introduction

1.1. Traditional steel production

The steel industry has a major role in the global economy and modern society. Despite the impact of the pandemic, just minor effects were felt in the steel industry at the end of 2020 [1].

Figure 1 shows the significant increase in crude steel production from 1950 to 2020. Around 1.435×10^9 tons of crude steel were produced in 2010, while 770×10^6 tons were produced in 1990, showing the importance of steel in modern society. When global economic growth slows or declines, the steel demand tends to follow the same trend [1, 2].

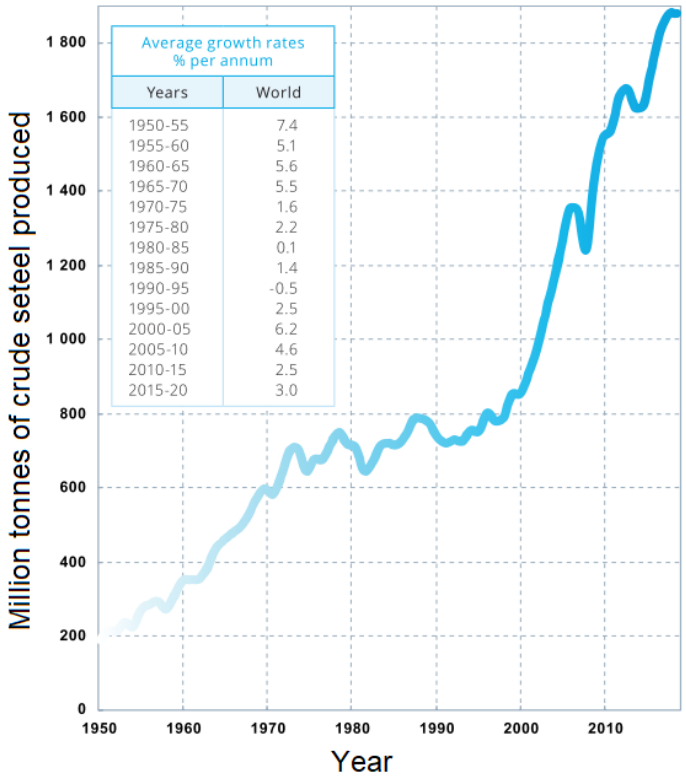

Figure 1: Crude steel production (million tons) [1].

Steel is the third most abundant man-made material, after concrete and wood, with an annual production of around 1.878×10^9 tons [2]. The wide range of applications of steel includes constructions, infrastructures, machinery, and consumer goods industries due to important features such as strength, toughness, low cost, and wide availability of iron ores [1, 2].

The main inputs to steelmaking are iron ore, energy (primarily coal, natural gas, and electricity), limestone and steel scrap. The metallic charge is made up of iron ore and scrap, with scrap having a significantly higher metallic concentration (>95%) than iron ore – typically in the range of 50-70%. It is required a metallic input of 1.1-1.2 tons to

produce a ton of steel. Steel production that uses iron ore as its primary source of metallic input is referred to as "primary", while scrap-based production is referred to as "secondary." [2].

Iron ores are constituted by several iron oxides, such as magnetite (Fe_3O_4) and hematite (Fe_2O_3), both with > 60% of iron content and goethite (FeO(OH)) with ~ 60% of iron content as the most commons. Less commons are limonite ($FeO(OH)\cdot n(H_2O)$) and siderite ($FeCO_3$) with ~ 50% of iron content [4]. For the iron oxide reduction to iron it is often used carbon monoxide and hydrogen as reducing agents. Most of these reducing agents are nowadays, generated from fossil fuel energy inputs, mainly coal and its derivative coke. Lime fluxes, such as limestone and dolomite, are used to remove impurities. Not only its production promotes carbon dioxide (CO_2) emissions, but the formation of slags (by-product) when chemically combined with the non-iron content of the iron ore [2].

Figure 2 represents a scheme for the raw material preparation, iron, and steelmaking, the three major stages of crude steel production.

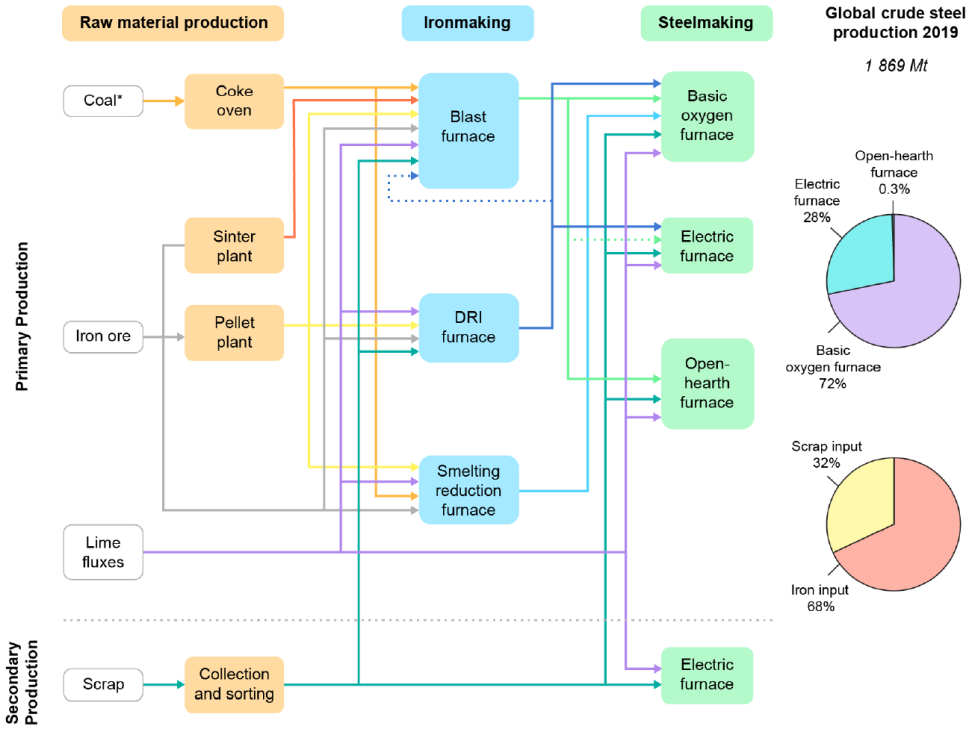

Figure 2: Main steel production routes and material flows in 2019 [2].

Iron ore must be previously processed for ironmaking, where ore fines need to be agglomerated by producing sinter or pellets. Heat and pressure are used in agglomeration processes to create nodules (sinter) and pellets, which can be stacked in a furnace, allowing gases to flow. Coke is heated up to about 1,100 °C, in the absence of air in a coke oven to remove volatile components, resulting in a mostly carbon-based substance [2].

The blast furnace-basic oxygen furnace (BF-BOF) route is the most widespread primary iron production pathway, accounting for roughly 70% of global steel production

and 90% of primary production. Coke and iron ore are introduced into the blast furnace from the top, while hot air, pulverized coal, or natural gas are injected into the lower part of the furnace. Thus, rising reducing gases meet descending iron ore. The production rate of the BF-BOF route is 15 GJ of energy input per 1 ton of liquid steel. Molten iron, also known as "hot metal", is produced in the blast furnace at temperatures of ~1,400-1,500 ºC. Then is introduced into the BOF, generally with scrap, to reduce the carbon content from ~4-5% to ~0.25%. In which, oxygen injection plays an important role to meet the required level for steel grade produced [2].

The direct reduced iron combined with the electric arc furnace (DRI-EAF) is another approach for steel production. The main characteristics of this route are [2]:

- DRI pellets are used with minimum impurities;
- reduction of iron ore to a solid-state in the DRI furnace, then melted in the electric arc furnace (EAF), typically with some scrap;
- between 18 to 30 GJ of final energy are required for producing 1 ton of steel.

BF-BOF and DRI-EAF routes represent 95% of global steel production. The remaining 5% is completed with three additional steel production routes still under development or outdated or for the production of special alloys [2].

All the processes related to steel transport, storage heating, handling and its transformation generate dust/particulate matter, SO_2, NO_x, small amounts of dioxins and metals. Life cycle assessment of steel arises as an important tool for a more sustainable steel industry [5].

Iron and steel production represent a high energy-intensive industrial activity due to the high abundance of iron ore and coal, but also to its increasing social demand. Greenhouse gas emissions are rising with the steel manufacturing increasing needs. To achieve a 50% reduction in carbon emissions, a 75% reduction of CO_2 emissions per ton of steel are needed, which may represent an issue for future steel production [1–3].

Global warming was mainly caused by the establishment of new industries and power plants, emitting harmful gases [6]. The reduction of CO_2 emissions, must be considered in the upstream steelmaking process, including mining, reduction, steelmaking, casting, and bulk-forming. According to the International Energy Agency, iron and steelmaking processes is equivalent to about 7-9% of the total world CO_2 emissions [3]. Stakeholders and policies require data trends about the demand, and amount of scrap available for recycling to develop tools for reducing significant emissions levels in the steel sector to decrease sectoral carbon footprints [2, 5]. To diminish this problem, the Paris Agreement was established in 2015 at the Conference of the Parties (COP) between 197 countries based on the United Nations Framework Convention on Climate Change (UNFCCC). The Agreement proposed the reduction of carbon emissions between those countries, to keep global warming below 2 ºC (ideally 1.5 ºC) above preindustrial levels [7].

1.2. Electrochemical deposition of iron oxides suspensions in alkaline media

As mentioned in chapter 1.1, the extensive energy consumption involved in the traditional carbothermal methods of steelmaking and the emission of the high amount of greenhouse gases such as CO_2 [8] reveal the urgency and relevance in the development of energy-efficient, carbon-free, and environmentally friendly solutions [9].

One of the possible routes investigated for a breakthrough reduction in greenhouse gas emissions are the electrochemical techniques, such as the alkaline electrolysis can be a promising process, for a greener iron and, consequently, steelmaking route. Thus, an iron oxide suspension or iron oxide cathode is used in an electrically conducting medium, such as an aqueous concentrated solution of sodium hydroxide (NaOH). The iron oxide reduction occurs at the cathode during the electrical current flow as well the hydrogen evolution, while oxygen evolution takes place at the anode (Figure 3) [8–10]. These chemical reactions occur because the electrochemical cell works with a higher external voltage than the open circuit cell potential [12]. Currently most of the studies are focused on the direct reduction of Fe_2O_3 particles suspended in a concentrated alkaline solution (~110 ºC), achieving current efficiencies of 70-80% [13–16]. Processed iron oxide-based pellets can also be used as cathodes, either as dense or porous, whereas the porosity showed to have a significant influence on the reduction rate and current efficiencies [9, 13–16]. Monteiro et al. [17] compared for the first time the reduction of dense and porous (45% of open porosity) Fe_3O_4 pellets, in an alkaline medium, reaching a current efficiency of 85% with porous samples due to the easy access of the electrolyte inside of the bulk pellets. The relatively low-temperature operation (~110 ºC) of the electrolytic iron production, combined with the production of hydrogen and oxygen as the only gases gained a lot of attention as a potential green alternative for the iron and iron-base alloy production [18].

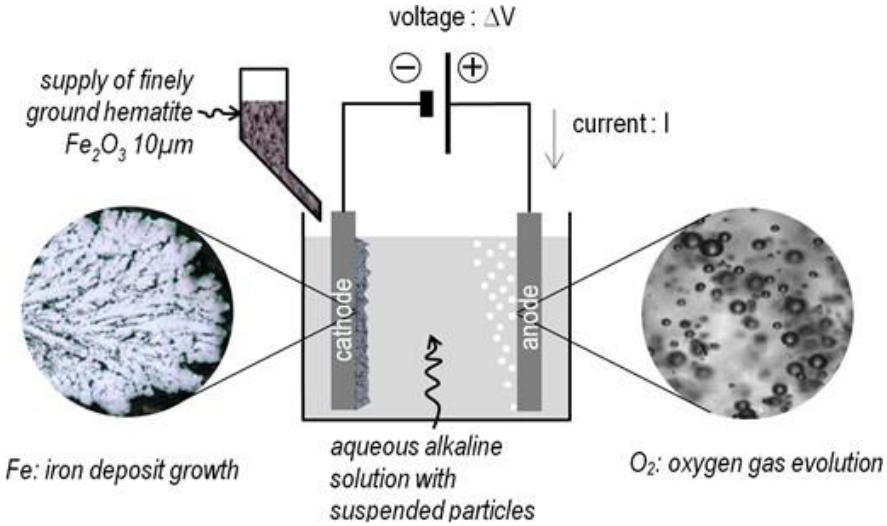

Figure 3: Electrolysis technology [19].

The main advantages of this technique compared to the traditional steelmaking plants are [19, 20]:

- A cut of the direct CO_2 emissions;
- The production rate is ~13 GJ of energy input per 1 ton of iron. Lower than the traditional carbothermal methods of steelmaking.
- Improved integration with renewable energies;
- It opens the possibility to produce steel from iron-rich products from residues.

Nevertheless, mass transport in aqueous solutions should be investigated, the electrochemical cell should be optimized and the reduction mechanism in different feedstocks should be performed in addition to the conventional Fe_2O_3 and Fe_3O_4 case studies [8].

1.2.1. Previous works on the reduction of iron from alkaline media

The iron oxide electrolysis to produce metal was shown by Lloyd in 1929 [21] and LeDuc et al. in 1959 [22].

Recent works were performed in the frame of EU projects such as the "Iron production by Electrochemical Reduction of its Oxide for high CO_2 mitigation" (IERO) and the "Ultralow CO_2 in Steelmaking" (ULCOS), in which demonstrated that more concentrated solutions improved the current efficiencies by spending less than 30% of the current in hydrogen evolution [10], leading to current efficiencies up to 70-85% for Fe_2O_3 suspensions [18, 22], 90-95% with iron purity above 98% [24]. On the other hand, the electrochemical reduction of other iron oxide feedstocks, such as Fe_3O_4 and α-FeOOH, obtain lower current efficiencies than Fe_2O_3 (Figure 4) [18].

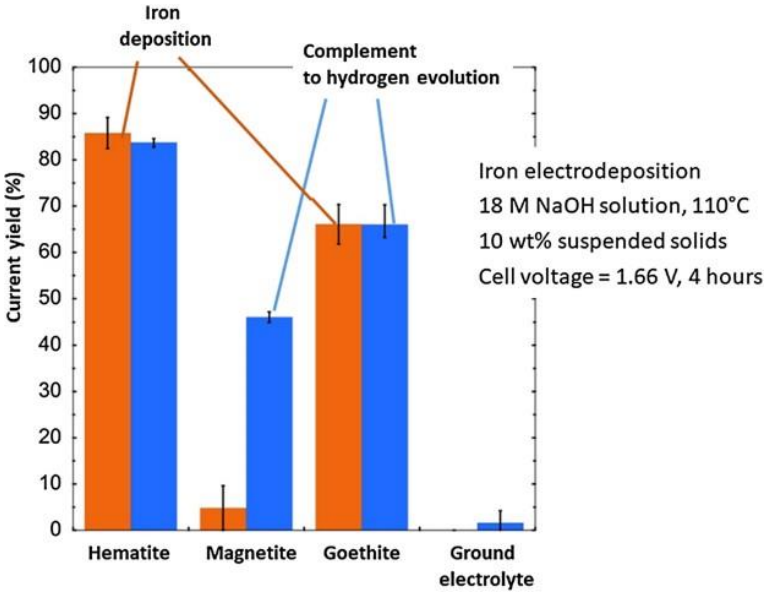

Figure 4: Current yield (%) of Fe_2O_3, Fe_3O_4 and α-FeOOH from iron deposition and complement to hydrogen evolution [18].

Further work has been targeting industrial needs, where researchers are seeking to produce iron from pre-treated bauxite residue (by-product of the alumina industry) suspensions (with HNO_3) in concentrated NaOH solutions, at 130 ºC with 20-30% Faradaic efficiency at higher current densities (250-1000 $A.m^{-2}$) and 50-70% at lower current densities (40-100 $A.m^{-2}$) [9, 11, 22, 24]. Due to the very complex chemical composition of the residue, Lopes et al. [26] mimic the main components of the waste from previously processed samples by emulsification of water suspensions in liquid paraffin, for studying the impact of the aluminum content during the iron oxides matrix reduction. The higher aluminum content in suspension negatively affects the Faradaic efficiency, as well as the quality of the Fe deposits. These results were obtained in the frame of the EU H2020 project SIDERWIN. With this solid foundation a 3-meter-long new experimental pilot scale cell was developed to validate this technology for Fe production [27].

1.2.2. Prospects of using a residue as iron oxide feedstock

In terms of iron-rich residue, such as the previously mentioned bauxite residue, also known as "red mud", it has a relatively high Fe_2O_3 content for potential steel production. Up to 95% of the alumina produced is obtained from bauxite extraction by the Bayer process. It is called “red mud” due to its red color from the high content in iron (III) oxide, due to the presence of 35 to 60% of Fe_2O_3 [9, 11] . The production rate in 2021 was approximately 140 million tons and has a tendency to increase [28].

The typical composition of Bauxite residue is shown in Table 1.

Table 1: Typical chemical composition of red mud [29].

Composition	Weight (%)
Fe_2O_3	30-60
Al_2O_3	10-20
SiO_2	3-50
Na_2O	2-10
CaO	2-8
TiO_2	Trace-25

Minor elements with smaller concentrations of the composition are critical and/or industrially important elements such as rare earth elements – REEs – primarily Ce, La, Sc, Y, Nd, and others [9].

Thus, red mud has been attracting some recent studies due to the SIDERWIN project, where some researchers have been trying to valorize it for the steel production [9, 11, 22, 24]. Demonstrating that iron reduction is possible with a by-product, such as red mud as feedstock.

Furthermore, sludges obtained from Ni electrolytic production can also be also considered for the iron electrowinning process. The current work is the first step of such process. In the scope of this thesis a by-product from Ni electrolytic production will be used as feedstock for steel production, called Nikkelverk Residue (NR).

However, it is not the only possible Fe source for the electrodeposition. There is a certain interest in the slugs obtained during metal refining. It was found that these materials can contain up to 25-40% of Fe_xO_y by mass.

1.3. Mechanism of the electrochemical reduction and deposition of iron oxides to iron from alkaline suspensions

1.3.1. Pure iron oxide mechanism

The electrochemical reduction of Fe_2O_3 occurs in the vicinity of the cathode or working electrode (WE) in the electrochemical cell and it is globally represented as (1):

$$Fe_2O_3 + 3H_2O + 6e^- \rightarrow 2Fe + 6OH^- \quad (1)$$

However, the electrochemical reduction and deposition consists of a two-step mechanism described as a reductive dissolution and electrodeposition, shown in Figure 5, where the iron aqueous species such as $Fe(OH)_4^-$ and $Fe(OH)_3^-$ are intermediary steps for the reduction to Fe^0 and its electrodeposition on the cathode.

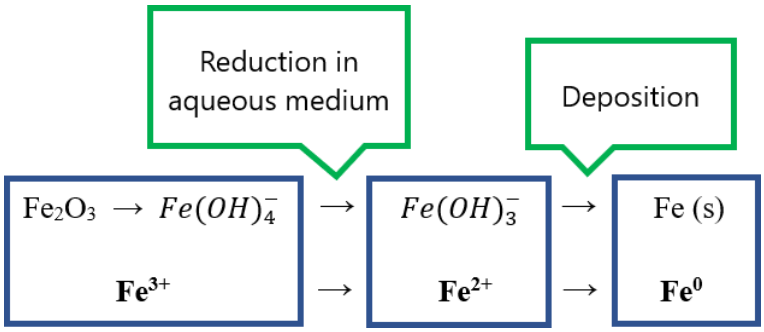

Figure 5: Two main phases of the electroreduction to iron.

The following schemes are represented from Figure 6 to Figure 10, showing in more detail the electroreduction mechanism of solid Fe_2O_3 suspended particles in alkaline media. Despite the low solubility of Fe_2O_3 in alkaline media (~1.1×10^{-3} M in 10 M of NaOH at 77 °C [30]), Fe_2O_3 particles are partially dissolved into $Fe(OH)_4^-$ aqueous anions in the electrolyte as an initial step and are represented in Figure 6 as Fe_{sol}(III).

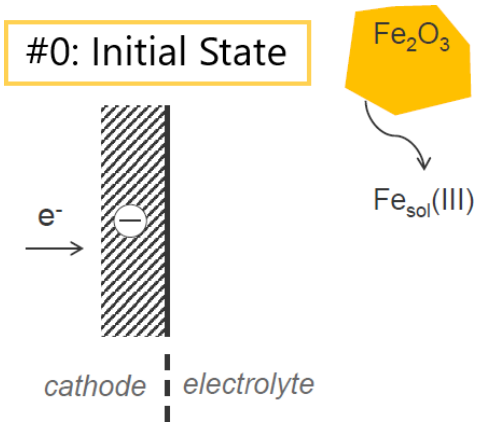

Figure 6: Initial state [27].

$$Fe_2O_3 + 3H_2O + 2OH^- \rightarrow 2Fe(OH)_4^- \quad (2)$$

Once the $Fe(OH)_4^-$ aqueous anions are formed, shown in (2), these species are reduced to Fe(II) species as $Fe(OH)_3^-$, shown in (3). The next step consists of the electroreduction of the Fe(II) aqueous species ($Fe_{sol}(II)$) into Fe^0 on the cathode, as shown in Figure 7 and eq. (4).

$$Fe(OH)_4^- + e^- \rightarrow Fe(OH)_3^- + OH^- \quad (3)$$

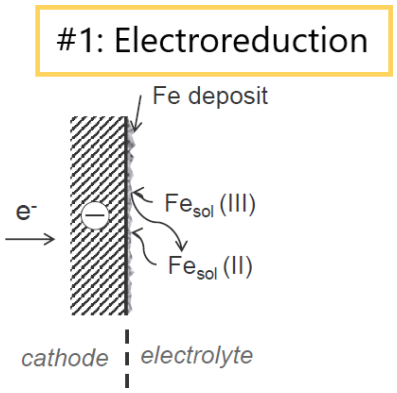

Figure 7: Electroreduction of soluble iron ionic species [27].

$$Fe(OH)_3^- + 2e^- \rightarrow Fe + 3OH^- \quad (4)$$

Other Fe_2O_3 particles in the WE vicinity promote an extra supply of iron oxides for further dissolution and reduction to $Fe_{sol}(II)$ as shown in Figure 8. Consequently, more $Fe_{sol}(II)$ in the aqueous solution will be reduced and deposited as Fe^0 on the cathode.

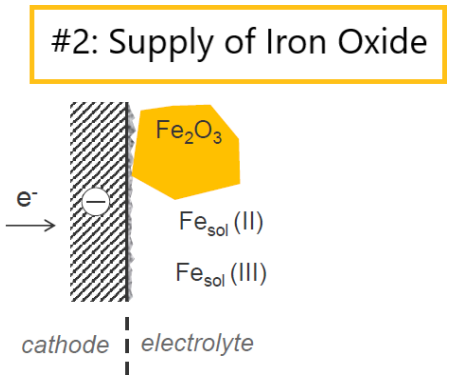

Figure 8: Supply of Iron Oxide [27].

In bulk pellets, Fe_2O_3 is reduced to Fe as shown in Ref. [31]. According to the Pourbaix diagram of iron species [32], Fe_3O_4 appears as an intermediary phase during the reduction of Fe(III) to Fe(II), confirming the presence of Fe_3O_4 throughout the electroreduction. However, in the electroreduction from iron oxide suspensions, the same is not mentioned in literature.

Attending to the Pourbaix diagram shown in Figure 9 and to some literature studies [17, 25], other possible aqueous Fe(II) species formed could be iron oxyhydroxide anions, $HFeOH_2^-$, in addition to $Fe(OH)_3^-$. The red line marks the typical electrolyte pH used in the electrochemical reduction of iron oxides to iron, where one can observe the presence of Fe_3O_4 and $HFeOH_2^-$ at lower potentials than -0.8 V vs. SHE.

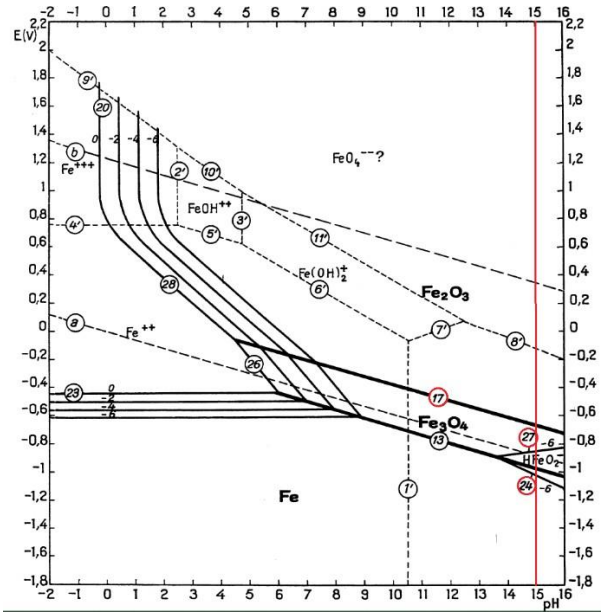

Figure 9: Potential-pH equilibrium diagram for the system iron-water, at 25°C (considering as solid substances only Fe, Fe_3O_4 and Fe_2O_3) [32].

The redox mechanisms related to the Fe deposition from Fe_2O_3 suspensions are shown in the cyclic voltammetry (CV) in Figure 10, recorded at 10 $mV.s^{-1}$ and 1,000 rpm of stirring. The CV shows that iron reduction can be achieved with a very small current and confirms the reactions involved in the overall process, as mentioned previously. The

first reaction to occur is the reduction of ferric ions (Fe^{3+}/Fe^{2+} – Reaction 3), at the plateau Cl, at -900 mV/SHE and a limiting current density of 1 $mA.cm^{-2}$. Finally, takes place the reduction of ferrous species, at -1150 mV/SHE (Fe^{2+}/Fe^{0} – Reaction 4). However, the iron deposition is hardly distinguished by the CV because of the hydrogen evolution (-1250 mV/SHE). Then at -750 mV/SHE, occurs the oxidation of ferrous ions and the cycle restarts [10].

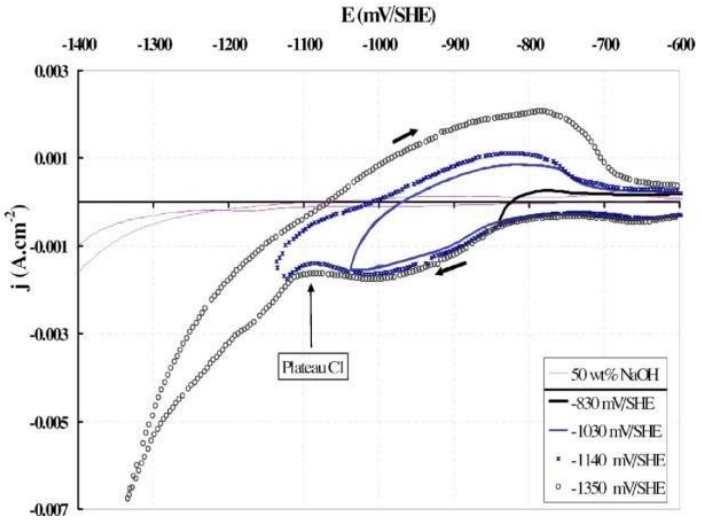

Figure 10: Voltammograms of dissolved iron solution in equilibrium with Fe_2O_3 [10].

1.3.2. The theoretical background of the process, Nernst equation

During the electroreduction and deposition of iron oxides to Fe^0 (Figure 11), hydrogen and oxygen gases are produced due to the water hydrolysis in the electrolyte. Hydrogen evolution reaction (HER), shown in (5), takes place on the cathode acting as a parasite current competing for the reduction to Fe^0 [13, 14]. At the anode or counter electrode (CE), oxygen evolution takes place.

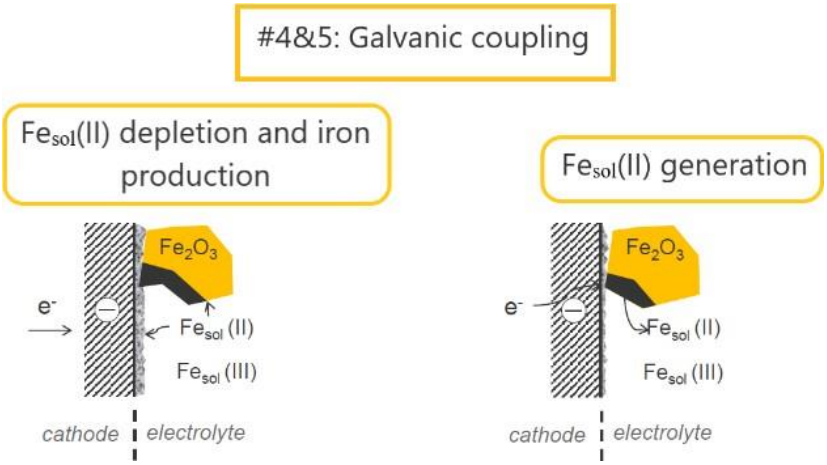

Figure 11: Galvanic coupling [27].

$$2H_2O + 2e^- \leftrightarrow H_2 + 2OH^- \quad (5)$$

In 1786 Luigi Galvani conducted the first electrochemical study, and Alexandro Volta developed the first electrochemical cell in 1799, consisting of two metal electrodes (Zn and Cu) immersed in sulfuric acid and salt bridge to connect them electrically. The Nernst equation (third law of thermodynamics), was created by Walther Hermann Nernst in 1887, being one of several reasons that he was awarded The Nobel Prize for Chemistry in 1920. Nernst equation can be used for many applications, such as determination of equilibrium constants, oxidation-reduction titration, pH dependence redox couple, between others. The electrochemical cell potential is defined by cathodic and anodic electrodes, in which reduction and oxidation semi-reaction occur, as the global electrochemical reaction. The equation (6) describes the ΔG (Gibbs free energy) of any reaction and the standard free energy change, ΔG° [34]:

$$\Delta G = \Delta G^0 + RT \ln Q \quad (6)$$

where Q is the reaction of mass action law. The galvanic cell also asks for a spontaneous global electrochemical reaction for a redox reaction, therefore the variation of Gibbs (G) is negative for a positive cell potential, as described by (7):

$$\Delta G = -\mathrm{z}FE \qquad \Delta G^0 = -\mathrm{z}FE^0 \quad (7)$$

Merging the equations (6) and (7):

$$-\mathrm{z}FE = -\mathrm{z}FE^0 + RT \ln Q \quad (8)$$

The Nernst equation can be obtained by rearranging the following equation $\left(Q = \frac{a_{Red}}{a_{Ox}}\right)$ [34]:

$$E = E^0 - \frac{RT}{zF} \times \ln \frac{a_{Red}}{a_{Ox}} \quad (9)$$

Where:

- E^0 is a standard electrode potential for the reaction (E_0 for H^+/H_2 = 0 V vs. standard hydrogen electrode – SHE);
- a_{Red} and a_{Ox}, the activities of the reduced and oxidized species respectively;
- R is the molar gas constant (8.314 $J.K^{-1}.mol^{-1}$);

- T is the temperature (in this case, 363 K);
- z is the number of electrons involved in a semi-reaction, or reaction if the cell is completed (2 in this case);
- F is Faradaic constant (96,485 C.mol^{-1}).

To observe how the pH can influence hydrogen evolution, three different pH values (3, 12 and 15) were used to calculate the respective potentials. As the gases activity in solution is usually taken by 1, and the number of electrons is constant, the equation can be presented for the hydrogen reduction as the following:

$$E = 0.0156 \times \ln(a_{H^+})^2 \quad (10)$$

Thus, the potential of hydrogen reduction at room temperature depends only on the activity of the H^+ ions. To find the activity in different solutions, the following equations will be used:

$$pH = -\log_{10}(a_{H^+})^2 \quad (11)$$

$$2H^+ = 10^{-pH} \quad (12)$$

It can be easily calculated that in solutions with pH 3, 12 and 15, the activities of H^+ will be 10^{-3}, 10^{-12} and 10^{-15}, respectively. Using equation (12), the potentials for hydrogen reduction in these solutions will be -0.216 V; -0.862 V and -1.078 V, respectively. Considering, that the potential of iron reduction is about -1 V, it can be concluded that Fe deposition is possible only in highly alkaline electrolytes. This is the main reason why such solutions were used previously [8–10, 13–15, 17]. In an acidic medium the evolution of hydrogen will be the main reaction to occur, hampering the reduction of iron oxides to Fe, especially due to the loop of iron valences between Fe^{3+} to Fe^{2+}.

1.3.3. Iron oxides as the feedstock of iron in the electrochemical cell

Recent studies on electrowinning technology have been carried out with iron oxides-hydroxides such as Fe_2O_3 [10], Fe_3O_4 [17] and α-FeOOH [18]. Fe_2O_3 is the most researched one due to its content in Fe(III), showing higher current efficiencies and cell current for similar electrolyte concentrations, temperature and applied potential [11].

Due to the Fe_2O_3 insulating properties (~10^{-14} S.cm^{-1}, room temperature [36]) against Fe_3O_4 (10^2-10^8 S.cm^{-1}, room temperature [18, 36]), one should take into consideration at least eight times higher current densities for the galvanostatic electroreduction from Fe_2O_3 suspensions when compared with Fe_3O_4. On the other hand, only two times higher current densities should be used for α-FeOOH (~10^{-6} S.cm^{-1} also at room temperature [18]).

Feynerol and his co-workers performed the first comparative study on the electroreduction of Fe from three iron oxide suspensions: Fe_2O_3, α-FeOOH, and Fe_3O_4 during their individual electroreduction with a NaOH electrolyte (18 M) [18]. Despite the extremely low electrical conductivity, an 85% current efficiency and 1100 $A.m^{-2}$ of current density were obtained with Fe_2O_3, when compared with the other iron oxide suspensions tested. On the other hand, a lower current density was obtained with α-FeOOH (650 $A.m^{-2}$), with 20% lower efficiencies than for Fe_2O_3, mostly due to the high viscosity of the electrolyte in contact with the FeOOH, which hampered the evolution of the O_2 bubbles. The lowest Faradaic efficiencies were obtained from Fe_3O_4 suspensions (5%) not only because of the higher contribution of the HER, visible by their thermodynamic redox potentials calculated in [18], but mostly due to the magnetic stirring used in the work, which hampered the availability of the Fe_3O_4 particles in the vicinity of the cathode, but it concentrates it at the bottom of the electrochemical cell. The latter was discussed by Lopes et al. [38] when trying to reduce a magnesium ferrospinel ($Fe_{2.3}Mg_{0.7}O_4$) to iron into a nickel grid, where Mg acted as a contaminant. The current efficiencies are usually lower when adding contaminants to the iron oxide matrix due to their coverage in the host spinel that blocks further reduction, by partly blocking the electrochemically active surface, showing kinetic limitations. Nevertheless, the Faradaic efficiencies attained 20% when using mechanical stirring instead of magnetic stirring, a higher value than the one obtained with pure Fe_3O_4 in [18].

In other works, different feedstocks were used such as the previously mentioned in chapter 1.2.2, red mud waste. Researchers Ahamed et al. [25] studied the viability of red mud in an alkaline medium at 110 ºC to produce electrolytic iron. The best faradaic efficiency was 72% at 41 $A.m^{-2}$, while only 20.5% was obtained at 1000 $A.m^{-2}$, against the 80% of current efficiency obtained with Fe_2O_3 for the same conditions. The researchers concluded that the presence of impurities such as cancrinite or perovskite, could affect the adsorption of the red mud particles on the cathode surface, not having the equivalent electrochemical reactivity when compared with the commercial Fe_2O_3. Lopes et al. [26] performed the electroreduction of iron in nickel grids from $Fe_{2-x}Al_xO_3$ suspensions, observing that the presence of alumina negatively impacted the morphology of the dendrites. Increasing the amount of alumina in suspensions, the Faradaic efficiencies were reduced from 70% (Fe_2O_3) to 32% ($Fe_{1.4}Al_{0.6}O_3$), due to a partial surface coverage with alumina-based precipitates.

The novelty of this work consists in using another iron oxyhydroxide feedstock for the first time, for iron electroreduction through alkaline electrolysis, the akaganeite (β- FeOOH). Moreover, one expects to valorize iron-rich residue from nickel production by the mentioned electrochemical approach for steel production, with high content of akageneite phase.

1.4. Experimental conditions

Recent studies on electrowinning technology focused on the experimental optimization of conditions regarding temperature, the concentration of the electrolyte, the load of iron oxide, stirring conditions, the composition of the suspensions, and electrode type.

The major developments in iron electroreduction from dissolved species in alkaline media have been performed since the 2000s. The typical electrochemical cell consists of polytetrafluoroethylene (PTFE) cylindrical beaker.

Allanore and his co-workers [10] worked with a volume of 400 cm^3 in a PTFE beaker incorporated in a stainless-steel cell with a two-wallet jacket. The electroreductions were carried out at a temperature of 110 °C in 50 wt% of NaOH electrolyte, with nitrogen bubbling to minimize the impact of oxygen in the electrochemical process. The electrochemical cell was composed of two anodes, a 50 cm^2 platinum cylinder, and a 130 cm^2 iron sheet (150 µm of thickness). A rotating disk made of pure graphite (1 cm^2) was used as the cathode – and Hg/HgO KOH (10 M) was used as the reference electrode. The role of the iron sheet anode was to investigate highly concentrated iron ions solutions due to some dissolution of the iron sheet to the electrolyte, thus increasing the iron concentration available in the solution.

The dissolution of Fe_2O_3 particles produced ferric species. Fe_2O_3 particles (10 g, 7.5 µm of average diameter) were added to the electrolyte and a porous diaphragm avoided the contact between Fe_2O_3 and the electrodes. After 3 h under 110 °C, the solution was found to be saturated with ferric species, with a concentration of $2.46 \times 10^{-3}\ M$, proving the dissolution of Fe_2O_3 in strong alkaline media.

Figure 12 shows the surface of the iron deposits. The metal deposited comprises regular and fine crystal aggregates with a size of ~1 µm.

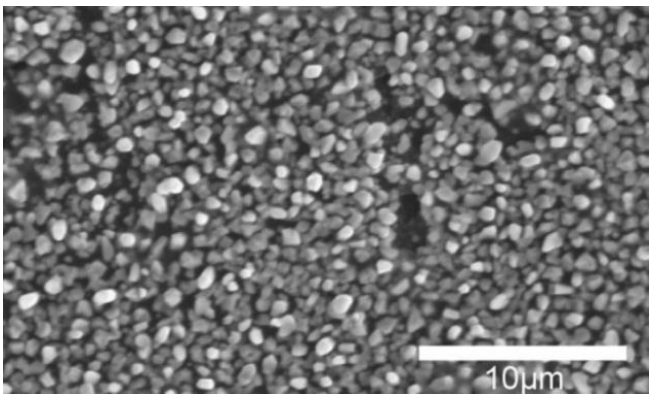

Figure 12: SEM image of Fe deposit on the graphite electrode [10].

Feynerol et al. [18] investigated the experimental conditions for the reduction of Fe_2O_3, Fe_3O_4 and α-FeOOH. Three electrodes were used inside of a cylindrical PTFE coated stainless-steel tank enclosed by a coil circulating calorific oil. One nickel anode was used, whereas a detachable graphite cylindrical rod served as a cathode. A reference electrode of Hg | HgO | KOH (1 M) monitored the anode and cathode potentials. The electrodes were immersed in a 1 M NaOH solution in a separate glass chamber. To keep the iron oxide-hydroxide particles suspended, the slurry was stirred magnetically at a rotational speed of 600 rpm. A 50 wt% NaOH electrolyte solution and 10 wt% of iron oxides or hydroxide as feedstocks were used. The slurry reached 110 ºC and by circulating nitrogen to the cell, the oxygen was removed. The electrolysis started in a fixed cell potential of 1.66 V for 4 h. The pressure in the cell was 60 mbar relative to atmospheric pressure.

Figure 13 shows the current density achieved during electrolysis for all chemicals at a cell voltage of 1.66 V. All three iron oxides demonstrated different profiles. Fe_2O_3 has the largest current density, averaging over 1000 $A.m^{-2}$. α-FeOOH steadily increases up to 700 $A.m^{-2}$, and Fe_3O_4 down to 150 $A.m^{-2}$, which is significantly less reactive. In addition, α-FeOOH electrolysis displayed faradaic efficiencies of around 20% lower than with Fe_2O_3. A possible explanation for this phenomenon could be some adsorption of iron oxides/hydroxides on the iron crystals preceded by the fact that iron can be generated on the cathode surface through the reduction of dissolved Fe(III) species. The low current density obtained with α-FeOOH may be explained by the high viscosity of the slurry.

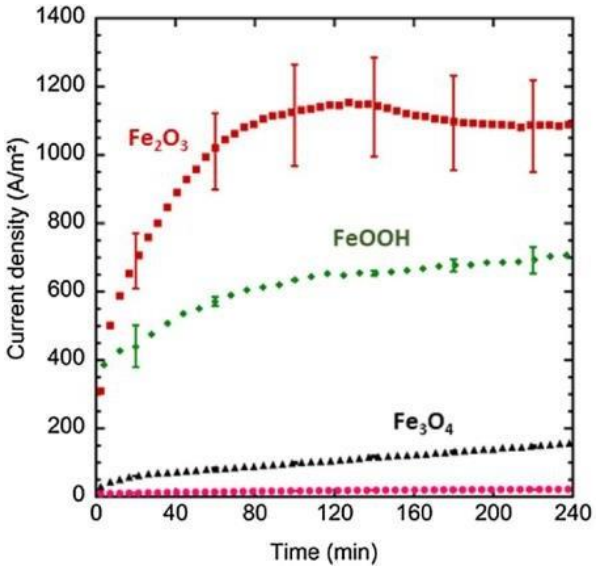

Figure 13: Current density vs electrolysis time for Fe_2O_3, α-FeOOH, Fe_3O_4 and NaOH–H_2O [18].

Figure 14 shows SEM images of the cathode surfaces after the electroreduction for a) Fe_2O_3 and b) α-FeOOH. Deposits of Fe from Fe_3O_4 suspensions are not shown because the particles were almost not visible, depositing less than 0.04 g. For Fe_2O_3, the average mass of the deposit was around 2.5 g. In the magnification x120, large nodules ranging in size from 300 µm to 1 mm were found, which are made up of bundles of smaller columnar crystallites (magnification x250, Figure 14 a)) ranging in size from 5 to 20 µm. At magnification x1000 the bigger crystals (10 to 20 µm) present a six-ridged star form. For α-FeOOH, 1 g of Fe was deposited and looked to be significantly denser than Fe_2O_3 deposits with a uniform rough surface. The Fe deposit from α-FeOOH shows smaller agglomerated spherical particles (magnification x250, Figure 14 b)) with a size between 10 and 20 µm and has a distinct morphology than the nodules formed by Fe_2O_3 [18].

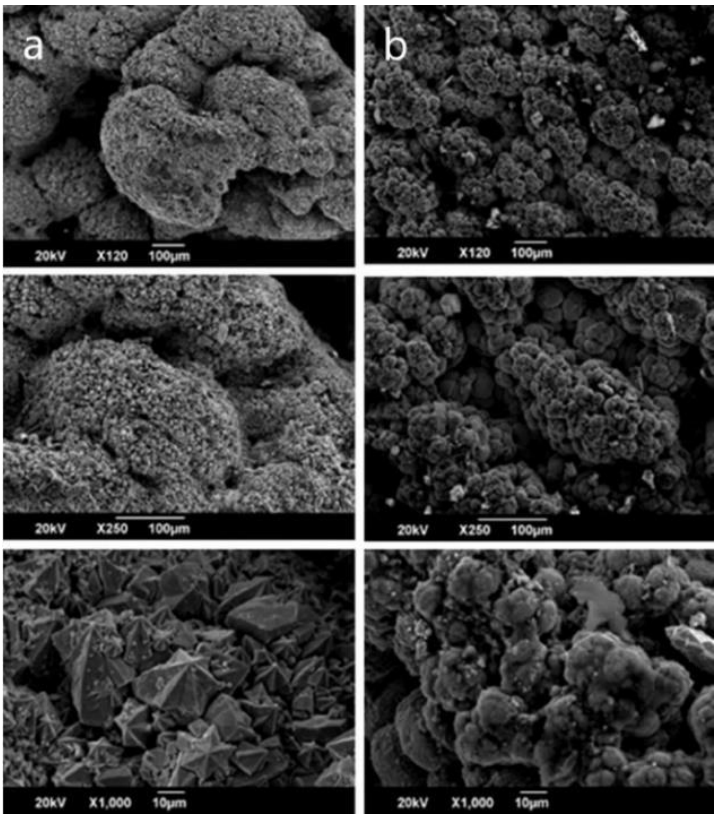

Figure 14: SEM microstructures of iron deposit from a) Fe_2O_3 and b) α-FeOOH [18].

Koutsoupa et al. [9] focused their study on the reduction of bauxite residue – red mud. The procedure was carried out in an electrolysis cell made with a 250 mL borosilicate glass beaker sealed with a specially designed cylindrical silicon bung. A three-electrode arrangement, as shown in Figure 15. The cathode and two anodes were shaped in rectangular plates, made of stainless steel and nickel, respectively. The surface area of the cathode immersed in the solution was 8 cm^2. A Hg | HgO | NaOH (1 M) electrode was utilized as a reference electrode.

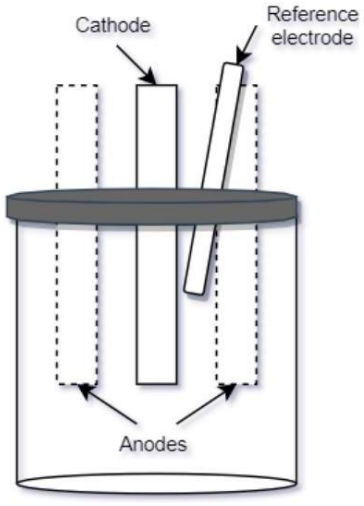

Figure 15: Electrolysis cell [9].

The stainless-steel cathode and nickel anodes were polished and rinsed with demineralized water before each experiment, afterwards, the cathode was weighed. The electrolyte was a 50 wt% NaOH aqueous solution, to which 10 wt% bauxite residue solid particles were added after 5 min of homogenization. To keep bauxite residue particles suspended, the slurry was stirred at a rotating speed of 500 rpm.

Koutsoupa et al. [9] concluded that the process temperature was the most significant parameter affecting the faradaic process efficiency. For the bauxite residue suspension at 130 ºC, a 72% faradaic efficiency was obtained.

1.5. Synthesis of β-FeOOH as a possible raw material for the electrochemical cell

1.5.1. β-FeOOH

While Fe_2O_3 has a corundum structure, particularly trigonal-hexagonal scalenohedral, Fe_3O_4 has an inverse spinel crystal structure, with Fe^{2+} and Fe^{3+} ions hosted in a cubic close-packed lattice array of oxide ions, in octahedral sites (O_h). Fe^{3+} ions can also be found in tetrahedral sites (T_d). However, none of them shows a tunnel structure as β-FeOOH [38, 39].

β-FeOOH is a Fe(III) (hydr)oxide with a chloride-filled tunnel structure, (2 x 2) channels, which refers to the width of the channels in octahedral units. The difference between α-FeOOH, apart from having a low crystalline iron hydroxide, is the crystal structure shown in Figure 16. α-FeOOH tunnel structure of (1 x 2) is characterized by polyhedral clusters of octahedron $Fe^{3+}O_3(OH)_3$, forming double chains with hydroxide ions along [001] [41].

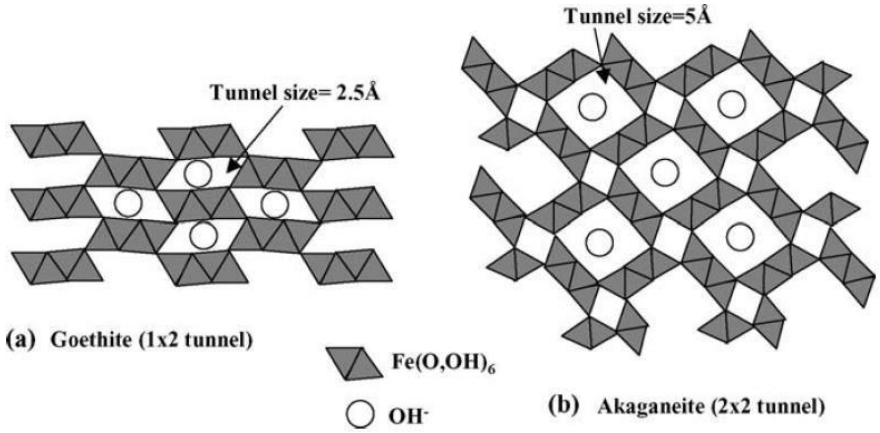

Figure 16: α-FeOOH and β-FeOOH polyhedral structures [41].

The existence of β-FeOOH as a corrosion product has previously been proven to be an effect of chloride-containing environments. However, attending to the research of Rémazeilles et. al [42], a significant amount of chloride in the media is insufficient to form this phase. It was shown that a high amount of dissolved Fe(II) ions is essential for the formation of the (hydro)oxide.

β-FeOOH is not common to be found in nature, but it can be formed under certain conditions, such as on the metal–oxide interface of iron materials or in a chloride-rich environment under acidic oxidizing conditions (pH 1–3), as a corrosion product of metallic Fe and Fe(II)-bearing solid phases and solutions [43]. It is also one among the main by-products of atmospheric corrosion of carbon steel in a maritime setting. In these conditions, hydroxychloride (β-$Fe_2(OH)_3Cl$) formation occurs, followed by its slow oxidation by the dissolved O_2 resulting in the composition of β-FeOOH. However, the oxidation of aqueous suspensions of β-$Fe_2(OH)_3Cl$ by air, results in the formation of the material called chlorinated green rust ($GR(Cl^-)$) as an intermediate product, which occurs before the formation of β-FeOOH [42].

The large specific area and tunnel structure of β-FeOOH shows to be promising for electrodes [44], catalysts [45], ion exchange materials, and adsorbents [46]. It has been widely employed as an adsorbent to remove pollutants from water, due to ease of handling, low cost, and excellent selectivity. Therefore, it is frequently encountered in corrosion products [41, 46].

There have been various reports on the Fe–O–H–Cl system phases into which β-FeOOH can be converted, such as FeOCl, α-FeOOH, and Fe_2O_3 [48].

1.5.2. Synthesis of β-FeOOH

When considering the use of β-FeOOH for the electrochemical deposition, one should synthetize it as a first approach, mostly to avoid electrochemical limitations by the presence of other non-conductive components present in feedstocks with a high number of phases in their chemical composition.

Synthetic β-FeOOH can be made by hydrolysis of Fe(III) or Fe(II) salts at various concentrations, pH, and temperature settings. β-FeOOH is synthesized commonly by hydrolysis of aqueous solutions of $FeCl_3$ (0.1–2 M) at moderated temperatures (40–120 ^oC) in an acidic (pH < 2) environment [43].

The synthesis from $FeCl_3$ can result in the presence of the chloride ions in β-FeOOH, which impose difficulties for the electrochemical application of β-FeOOH since it can oxidize on the cathode, leading to the formation of pure chlorine gas. However, on a laboratory scale, this phenomenon can be avoided by the separation of the electrolyte with a membrane. The procedure of β-FeOOH synthesis via $FeCl_3$ hydrolysis is simple and fast [47].

It is also possible to obtain β-FeOOH at higher pH values (4-6), by oxidation of Fe(II), as demonstrated by Rémazeilles et al [42]. Chitrakar et al [41] showed that even at pH 8-10, hydrolysis can be performed by gradual addition of the 0.1 M NaOH to a 0.1 M $FeCl_3$ solution at room temperature with intensive stirring. Deliyanni et al. [49] have reported that hydrolyses of the iron (III) chloride in the ammonium carbonate or ammonium carbamate medium resulted in the formation of a nanocrystalline precipitate to be constituted predominantly as β-FeOOH [44, 45]. The formation of needle-like β-FeOOH particles was reported by Nesterova et al. [51] by hydrolysis due to the presence of large acetylacetonate anions and Cl^- in the solution.

Sujimoto et al. [52] used NaOH and $FeCl_3$. The $FeCl_3$ solution was filtered via a membrane filter with a pore size of 0.2 μm before use, and it was prepared using distilled water. After 6 hours at 100 ºC, the amorphous $Fe(OH)_3$ particles were entirely transformed into needle-like β-FeOOH particles.

To reach the liquid-solid equilibrium, β-FeOOH particles were suspended in an alkaline medium for 24 hours at room temperature before starting the ageing process. Centrifugation at 18,000 rpm for 30 minutes separated each supernatant solution from the precipitate, which was then filtered through a membrane filter with a pore size of 0.2 μm. To precipitate the iron species as $Fe(OH)_3$, 10 mL of the solution was neutralized with ~ 5 mL of HCl. To complete the precipitation, the supernatant solution was removed by centrifugation at 18,000 rpm for 60 minutes after ageing for 24 hours at room temperature. The precipitate was then dissolved with 2.5 mL of concentrated HCl and diluted with distilled water. It was concluded that by adjusting the temperature during the precipitation of $Fe(OH)_3$ before the synthesis of β-FeOOH, the size of the product can be systematically regulated [52].

Rémeazeilles et al. [42] used a method of synthesis by precipitation of Fe(II) compounds from $FeCl_2 \cdot 4H_2O$ and NaOH solutions. To ensure a homogeneous oxidation, the suspensions were stirred at a constant temperature of 25 ºC. The oxidation leads to the complete transformation of the initial Fe(II) compound into $GR(Cl^-)$ at concentration ratios $R' = [Cl^-]/[OH^-]$ greater than 1.10. The product of the oxidation of $GR(Cl^-)$ could be β-FeOOH, for [NaOH] = 0.4 mol/L and $R' \geq 8$. β-FeOOH was found solely in $FeCl_2$ solutions, indicating that both Fe(II) and chloride concentrations are critical for the synthesis of this compound. It was proven that only the kinetics of the reaction was affected by the oxygen flow, with β-FeOOH being produced from $\beta\text{-}Fe_2(OH)_3Cl$ via $GR(Cl^-)$ after 6 or 50 hours, depending on the oxygen flow, given that both $[Cl^-]$ and $[Fe^{2+}]$ were crucial [42].

Zic et al. [52, 53] investigated the crystallization from dense β-FeOOH suspensions to Fe_2O_3 particles. The experimental conditions for the preparation of the β-FeOOH suspensions are shown in Table 2.

Table 2: Experimental conditions for β-FeOOH solutions [54].

Sample	$FeCl_3$ (M)	NaOH (M)	T (ºC)	Ageing time (h)
S1	1	2.7	90	24
S2			120	2

The concentration of $FeCl_3$ and NaOH solutions was the same as when concentrated solutions were mixed. For about 10 minutes, the dense suspensions were vigorously stirred. The homogeneous suspension was placed in a Teflon-coated, non-stirred pressure vessel (autoclave). The autoclaving temperature was set to 90 and 120 ºC, and the mother liquor was separated from the precipitate using an ultra-high-speed centrifuge after cooling the autoclave. After washing with distilled water to remove "neutral electrolyte", the precipitates were dried at 60 ºC [54].

1.6. Objectives and motivation for the thesis

This master thesis, in collaboration with the European project SIDERWIN under the Horizon 2020 support (SIDERWIN-DLV-768788 – Horizon 2020/SPIRE10), within the framework of the valorization of an industrial iron-rich residue by electrodeposition for steel production without CO_2 emissions. The industrial iron-rich residue chosen for this study was a by-product of the nickel production from a Norwegian company, Nikkelverk. The main phase of this by-product is an iron oxide – β-FeOOH. Thus, the mentioned energy-efficient and carbon-free methodology of steel production is planned to be applied for the first time on the direct reduction of β-FeOOH particle suspension in a strong alkaline solution at low temperature (~100 ºC). Other iron oxides such as Fe_2O_3, Fe_3O_4 and α-FeOOH, have already been studied on this matter in several scientific articles. β-FeOOH material, however, is yet to be investigated for this purpose, thus it is a huge motivation and challenge to be the first ones to study this material for this application.

As discussed previously in the introduction, the steel industry is the most energy-intensive industrial activity, releasing high concentrations of greenhouse emissions to the atmosphere. Thus, with the establishment of the Paris Agreement, is imperative to find an energy-efficient, carbon-free, and environmentally friendly solutions. Here enters the electrochemical techniques, such as alkaline electrolysis, that cuts the direct CO_2 emissions, and it opens the possibility to produce steel from iron-rich products from residues. So, the main motivation is to investigate this technology using residues and share the results with the scientific community to promote and encourage scientists to follow this idea to an ultimate goal: a "greener" and more sustainable world.

The main objective of this dissertation is to obtain good Faradaic efficiencies and reproducibility for the electrochemical deposition of alkaline suspensions based on the NR and compare the results with other iron oxides.

The objectives of this thesis are:

- Synthesize and characterize the main composition of the NR;
- As a first approach, the production of Fe by electrochemical deposition of alkaline suspensions based on the synthetic β-FeOOH was evaluated. Following by the suspensions based on Fe_2O_3 and NR.
- Compare the electrodeposition of the synthetic iron-(hydro)oxide suspensions with the industrial iron-rich residue.
- Study the factors affecting Faradaic efficiencies, such as the temperature, the NaOH concentration, the β-FeOOH load on the solution and the material suspended in the solution were studied.
- Investigate the electrodeposition mechanisms and establish the main factors affecting the Faradaic efficiency.

2. Experimental procedure

2.1. Synthesis of β-FeOOH

Two methods were selected for the synthesis of β-FeOOH, the hydrolysis with sodium hydroxide and the hydrolysis with urea and ammonia, as described before.

2.1.1. Hydrolysis with sodium hydroxide

The hydrolysis was performed in 50 mL of 0.1 M iron chloride ($FeCl_3$) (PanReac AppliChem ITW Reagents) solution in distilled water. A 200 mL of 0.1 M sodium hydroxide (NaOH) (Sigma-Aldrich, 97%) was then added drop by drop to obtain a pH equal to 10, at room temperature. The color of the mixture was found to be changed from light brown to darker red. Then the solution was filtrated to obtain the β-FeOOH, attending to the chemical reaction (13).

$$FeCl_3 + 3NaOH \rightarrow FeOOH + H_2O + 3NaCl \quad (13)$$

The powder is then dried in the oven at 60 ºC for 24 hours.

2.1.2. Hydrolysis with urea and ammonia

In the second method, hydrolysis was also performed in 1.5 L of 0.33 M of $FeCl_3$ mixed with 1 M of urea (CH_4N_2O). About 5 mL of ammonia hydroxide solution (NH_3) (Honeywell Fluka™) was added to adjust the pH of the solution to 1.5. The solution was heated at 100 ºC and mixed with a magnet for 6 hours. The color changed from dark red to brownish, as shown in Figure 17. The powder was washed in a ventilated centrifuge (Mega Star 1.6R) for ten cycles of 10 minutes at 4000 rpm. Finally, the powder was dried at 60 ºC overnight.

$$FeCl_3 + 3OH^- \rightarrow FeOOH + H_2O + 3Cl^- \quad (14)$$

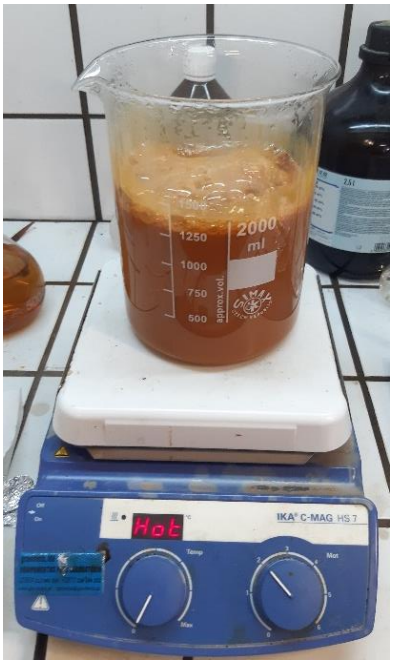

Figure 17: Hydrolysis of $FeCl_3$, CH_4N_2O and NH_3.

2.2. Scanning Electron Microscopy with Energy Dispersive Spectrometer

The morphology of the iron (hydro)oxide powders and iron deposits were studied by Scanning Electron Microscopy (SEM) with a Hitachi S4100, while the chemical characterization was performed by Energy-dispersive X-ray spectroscopy (EDS) with a Hitachi SU-70 using a Bruker Quantax 400 detector.

Scanning Electron Microscope (SEM) obtains high spatial resolution and field depth images (of around 10-15 Å) using a very low wavelength electron beam manipulated by electromagnetic fields, changing the direction of propagation by the creation of magnetic fields. This is possible because the electrons have an electric charge, and thus can be accelerated with a potential difference. Occurs a high variety of signals produced such as electron beam, elastic, inelastic and non-dispersive transmitted electrons, auger, secondary and retro dispersed electrons, continuous and characteristic X-ray, and heat [55–57].

Energy-dispersive X-ray spectroscopy (EDS) obtains the elemental composition of the sample by the use of an X-ray detector that absorbs all the variety of signals previously described. The energy analyzer converts these signals into voltages that relates to the characteristic X-rays of a specific element [55].

To prepare the samples for SEM/EDS, the cathode was glued with carbon glue and carbon tape to the sample holder with extreme care to avoid the disintegration or the contamination of the iron deposited. At last, glue dried overnight.

SEM/EDS was used in the present work to study the microstructure and eventual chemical composition of the iron deposits. Both microscopes used for the thesis are shown in Figure 18.

Figure 18: Hitachi S-4100 and Hitachi SU-70 Scanning Electron Microscopes, respectively.

2.3. X–Ray Diffraction

X-Ray Diffraction (XRD) technique was used to analyze the structure of both initial iron oxides and obtained iron deposits, and to study their composition. Diffraction process reveals the interior of crystals by bombarding materials with radiation that has a shorter wavelength than the distance between atoms (d_{hkl}). An X-ray beam is scattered by a crystal in a large number of different directions. Each scattered beam is the result of a reflection on a group of parallel lattice planes with the indices h, k, and l. This is theoretically clarified by the Bragg Law (equation (15)), where d is the distance between the parallel planes, θ the reflection angle, λ the X-ray wavelength and *n* diffraction order (Figure 19). The X-ray diffraction is the result of constructive and destructive interferences between waves resulting from coherent (no change in the λ of the wave) interactions with atoms [58, 59].

$$2d \sin\theta = n \times \lambda \tag{15}$$

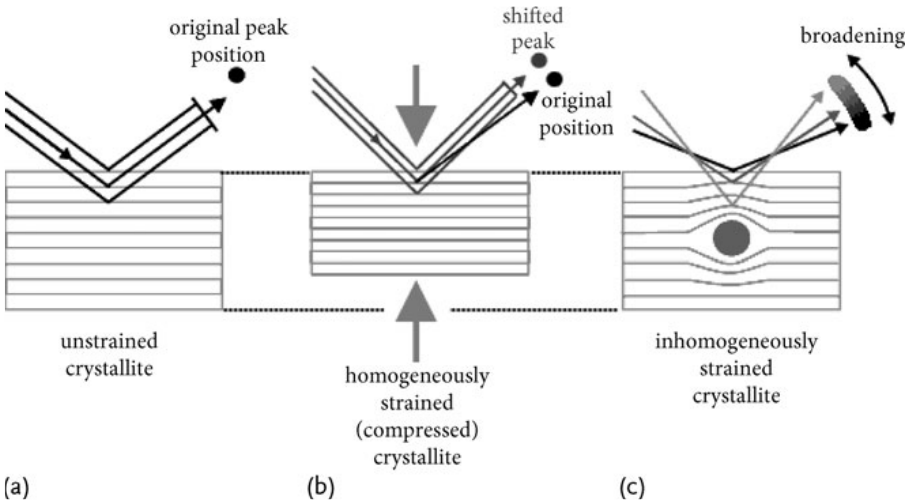

Figure 19: Effect of the crystal strain in the diffracted signal [60].

X-ray diffraction determines the crystal structure and the degree of atomic organization, the preferred crystallographic orientation of the crystals, its size, internal size and internal strain state and it identifies the phases composition.

Phase composition of powders and iron deposits was studied with a PANalytical XPert PRO diffractometer (CuKα radiation, 2θ = 10-80º) with a graphite monochromator. The phase identifications were accessed with a Panalytical HighScore Plus 4.7 (PDF-4) software. The measurement conditions used for the XRD analysis are described below:

- (Continuous) Scan step time of 16 minutes and 30 seconds;
- Range from 10 to 80º (2θ);
- Step of 0.05º (2θ);
- Temperature = 25 ºC;
- Monochromator – selection of a single λ;
- I = 40 mA and V = 45 kV.

The X-ray diffractometer is shown in Figure 20.

Figure 20: X-ray diffractometer.

2.4. X-Ray Fluorescence spectroscopy

Similarly, to XRD, X-ray Fluorescence spectroscopy (XRF) was used to investigate the chemical composition of the materials used in the current work, named OmnianHélio (PElements). In contrast to XRD, this technique allows for the analysis of substances which have an amorphous structure, thus they do not generate well-defined diffraction peaks. XRF is a technique based on the photoelectric effect (fluorescence process) to obtain a quantitative analysis of the chemical elements by examining the X-ray spectra emitted by the sample.

The principle of X-ray fluorescence, shown in Figure 21, is the ejection of electrons as photoelectrons due to the irradiation of high-energy X-photons on the sample atoms. This promotes “holes” in orbitals converting atoms into ions, which are filled by electrons from outer orbitals. To give the atom its initial stability, this transition is followed by the emission of a secondary X-photon with the energy equal to the difference between the initial and final levels. It is possible to identify the atom by comparing the energy of the fluorescence (or secondary) X-photon to the energy required for the quantum leap (characteristic X-ray).

Known as the fluorescence phenomenon, each element has its characteristic transition, depending on the characteristics of the beam, powder particle size distribution and compounds in the matrix [61].

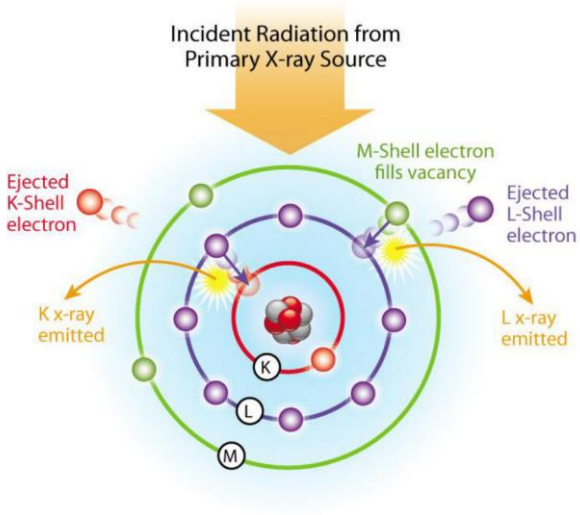

Figure 21: X-ray fluorescence principle [61].

2.5. Coulter particle size distribution analysis

The study of the particles size distribution of both samples was performed using a Coulter^{TM} LS230 laser. It measures the size distribution of suspended particles by the scattering of a 750 nm wavelength laser light, established on Fraunhofer diffraction theory, using the principle of laser scattering. As shown in Figure 22, the instrument is equipped with a laser, a projection lens (giving the laser beam constant intensity), a single Fourier lens (avoiding the use of more than one lens, as demanded in some alternative instruments) and an additional detector array to measure the polarization intensity

differential scattering (PIDS) of light. Between these last two items, powder suspended in a fluid (most cases water) runs through an orifice in the path of the laser beam, scattering it. This technique uses a single frequency polarized light beam scattered onto six detectors to measure particles down to 0.04 μm. It is a non-destructive and fast technique [62].

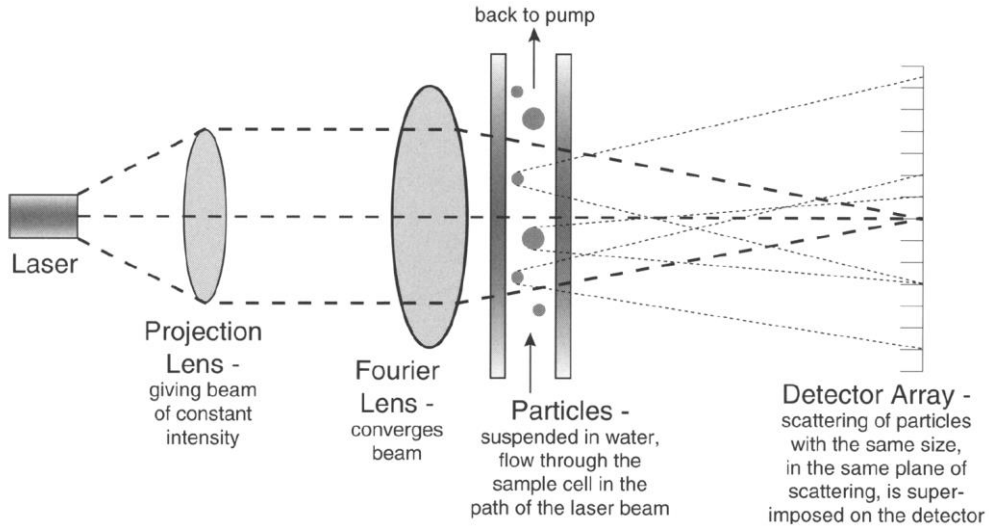

Figure 22: Schematic diagram of the Coulter TM LS230 laser granulometer optical system [62].

2.6. Preparation of the cathodes

The cathodes used are made of raw steel. The tips were cut using a guillotine and polished using a diamond polisher disk machine to become cylindrical. Before use, it was washed with ethanol to remove the impurities using a DREMEL 4000. The equipment is shown in Figure 23.

Figure 23: Diamond polisher disk machine and DREMEL 4000.

2.7. Electrochemical cell and measurements

The electrochemical cell is a cylindrical PTFE beaker composed of three electrodes shown in Figure 24:

• Reference electrode (Hg | HgO – KOH 1 M).

• WE (cathode) – Raw steel rod, area of a cm^2 immersed in the electrolyte.

• CE (anode) – Nickel plate, area of 2 cm^2 immersed in a NaOH solution (10/18 M).

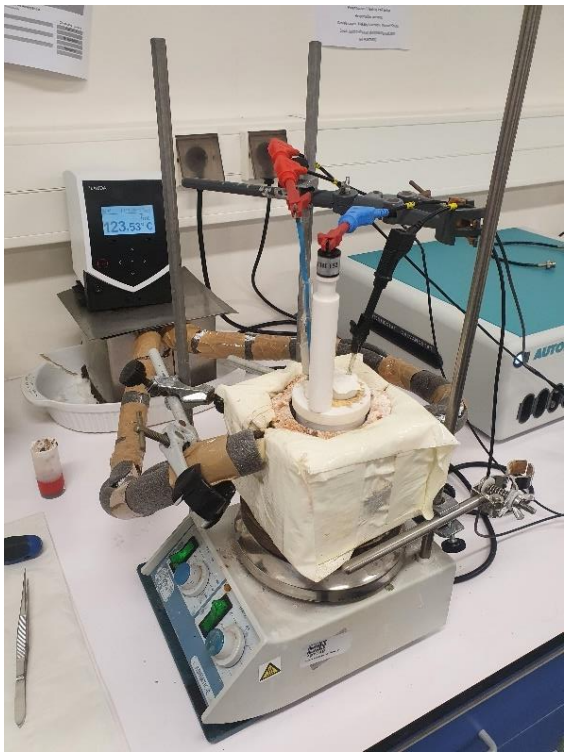

Figure 24: Electrochemical cell and heating system.

The alkaline suspensions of synthetic β-FeOOH and industrial iron-rich residue (100 g/L for each case) were prepared in 10 and 18 M NaOH electrolyte solutions. The 18 M solutions were used when increasing the temperature of the electrochemical reduction was necessary, attending to the boiling point of the electrolyte. Moreover, one expected also diminish the H_2 evolution at the same applied potentials in the latter case [24].

The electrodepositions were performed at 90, 105, 120 and 130 ºC. To keep the iron oxide-hydroxide particles suspended, the slurry was stirred magnetically at 200 rpm. Both the cathode and reference electrode were immersed in the solution, whereas the anode was immersed in a solution of 10/18 M of NaOH in a separate module, inside of the same electrochemical cell (Figure 25). A commercial membrane ZIRFON (Agfa) was added to the separate module for preventing eventual mixtures between both solutions to avoid the generation of chlorine gas in the anode. ZIRFON membrane is a zirconia-based membrane with a polymeric matrix often used for alkaline electrolysis for gas separation purposes.

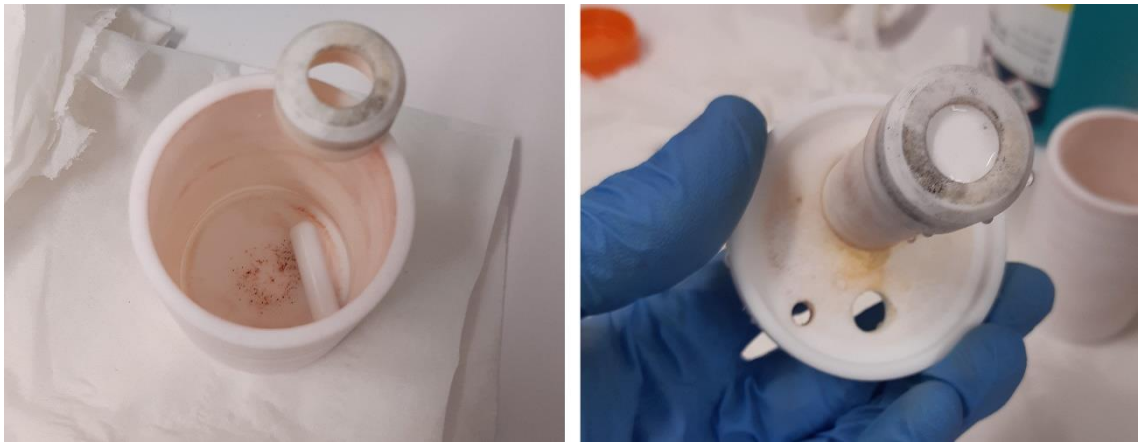

Figure 25: Images of the main and separate module of the electrochemical cell, showing the ZIRFON membrane.

The purpose of this setup was to study the mechanisms of the electrochemical reduction of iron-(hydro)oxides into Fe and the Fe deposition on the cathode, and its influence on the Faradaic efficiency in all the tested compositions.

2.7.1. Heating thermostat

To control the temperature of the solution, a Lauda heating thermostat (Figure 26) was used to pump heat silicone oil through a tube to an electrochemical cell jacket.

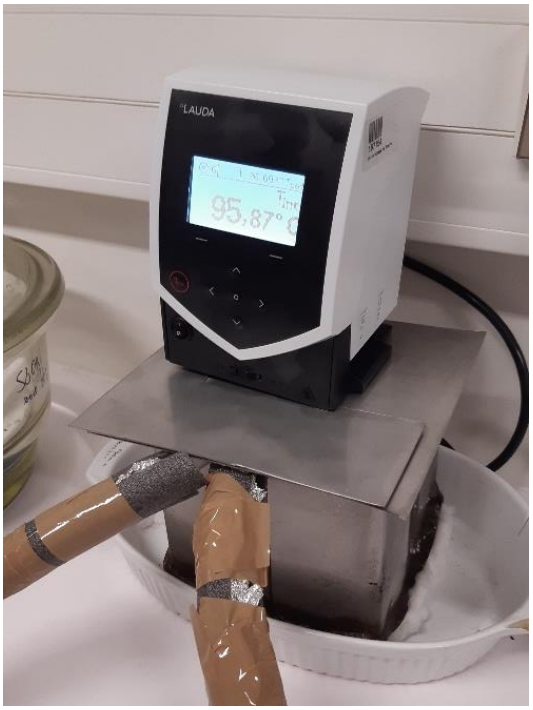

Figure 26: Lauda ECO heating thermostat.

2.7.2. Potentiostat

The Metrohm Autolab PGSTAT302N (Figure 27) was used to perform electrochemical tests. It features a wide measurable range of current and potential, and the use of NOVA software to control all the experimental aspects of the analysis. This specific model has a maximum current of 2 A, and a compliance voltage of 30 V which is required for the deposition in nonconventional solutions used in the current work [63].

The electrochemical tests performed were chronopotentiometry, chronoamperometry and cyclic voltammetry. The chronopotentiometry and chronoamperometry measurements took 16 hours. The chronopotentiometry measured the variation of applied potential (V) with constant current density of -0.025 $A.cm^{-2}$. Whereas the chronoamperometry measured the current density variation with an applied a voltage of -1.075, -1.10 or -1.15 V. The cyclic voltammetry shows the redox reactions of the sample by measuring the current density variation along the potential range of [-1.5, 0.8] V for four cycles.

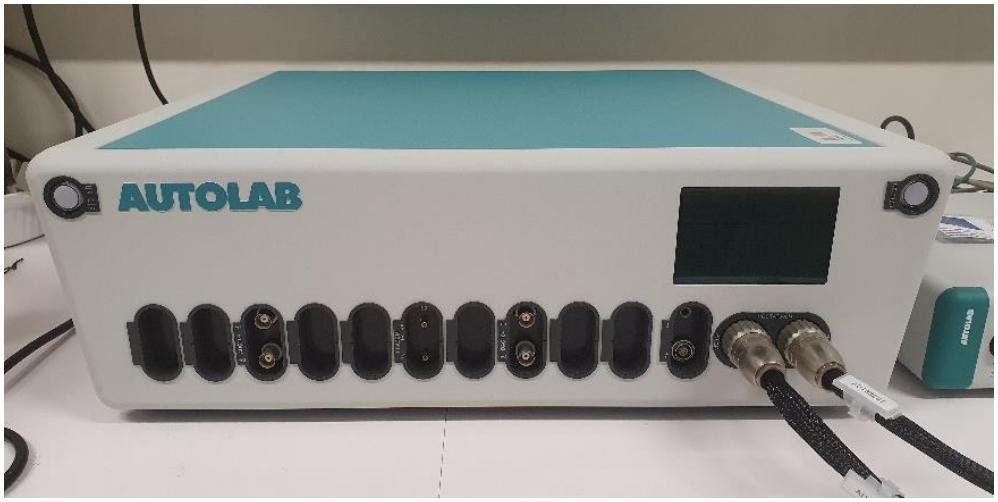

Figure 27: AutoLab Potentiostat/Galvanostat.

2.8. Faradaic efficiency calculation

The faradaic efficiency ($\eta_{fararadaic}$) of each electrochemical process performed was calculated as in equation (16).

$$\eta_{faradaic} = \frac{\Delta m \times z \times F}{M_{Fe} \times Q} \quad (16)$$

The variables from eq. (16) are described below:

- Δm – mass difference of the cathode before and after the electrochemical depositions (g);
- z – number of electrons (3 electrons in the present case);
- F – Faraday's constant (96485 $C.mol^{-1}$);
- M_{Fe} – molar mass of iron (55.85 $g.mol^{-1}$);

- Q – electrical charge passed through the cell.

The electrical charge (Q) was calculated based on eq. (17), depending on the usage of a stable or variable current over time (galvanostatic or potentiostatic mode, correspondingly), where the total duration of the experiment is represented by t, in seconds (57600 s), and I is the absolute current in A. The fixed current used was typically of -0.025 A.

$$Q = I \times t(fixed\ current)\ or\ Q = \int_0^t I\ dt(variable\ current\ over\ time) \qquad (17)$$

3. Results

3.1. Characterization of the synthetic β-FeOOH, NR and Fe_2O_3 powders

The materials under study in the present Thesis are the synthetic composition of synthetic β-FeOOH, the residue from NR and Fe_2O_3.

3.1.1. Cumulative particle size distribution analysis

Figure 28 represents the cumulative size distribution analysis of particles, where D50 values represent the particle size diameter (μm) that corresponds to a cumulative 50% of the particles of each composition. Thus, 50% of each particle composition have diameters lower than 1.859, 1.096 and 0.564 μm for β-FeOOH, NR and Fe_2O_3, respectively. Fe_2O_3 revealed to have the smallest D50 value.

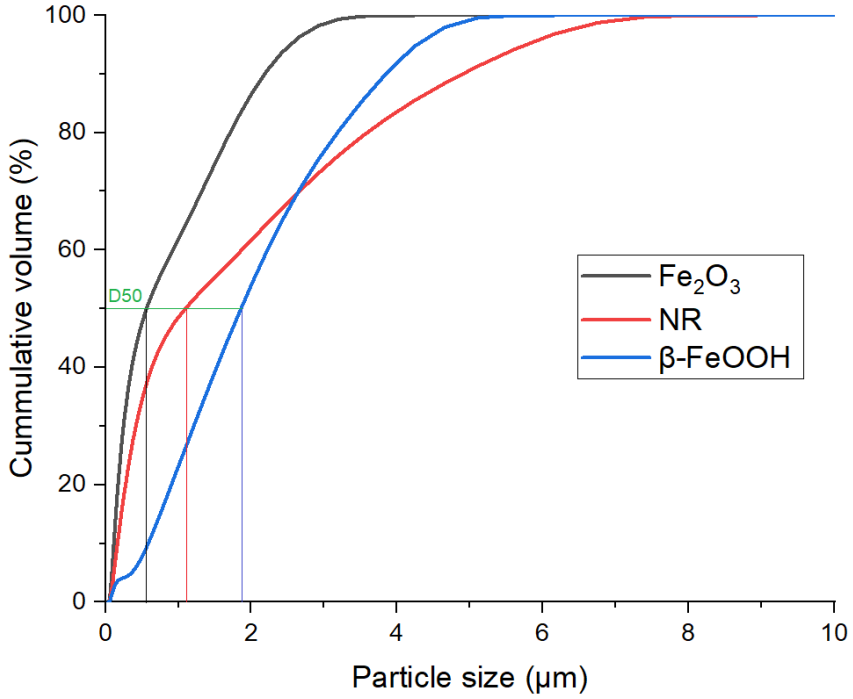

Figure 28: Granulometric distribution analysis of β-FeOOH, NR and Fe_2O_3.

3.1.2. Phase identification by XRD analysis

Two different methods were performed for the β-FeOOH synthesis seeking the purest single β-FeOOH phase formation. Moreover, different drying temperatures of the final powder were tried for optimization purposes. The XRD analysis of the obtained powders is presented in Figure 29. While the first method was based on the hydrolysis with sodium hydroxide (chapter 2.1.1), the second was based on the hydrolysis with urea and ammonia (chapter 2.1.2). Both the powders were dried in the oven overnight at 60 and 200 ºC.

The XRD analyses of the final powder obtained from the first method showed broad peaks on both diffractograms, indicating poorly crystalline phases at both temperatures. Moreover, the presence of $Fe(OH)_3$ impurity was found at 60 ºC. Higher temperatures (200 ºC) lead to a complete thermal decomposition of β-FeOOH into Fe_2O_3. On the contrary, the second synthesis resulted in the formation of a more crystalline material as one can see in Figure 29. A minor phase of iron (III) oxide was found at 60 ºC. Partial thermal decomposition of β-FeOOH to Fe_2O_3 is present in the diffractogram when the powder was heated up to 200 ºC. Considering the previous results, the second synthesis method was selected for further studies in the present Thesis. The powder was dried at 60 ºC overnight in all subsequent experiments.

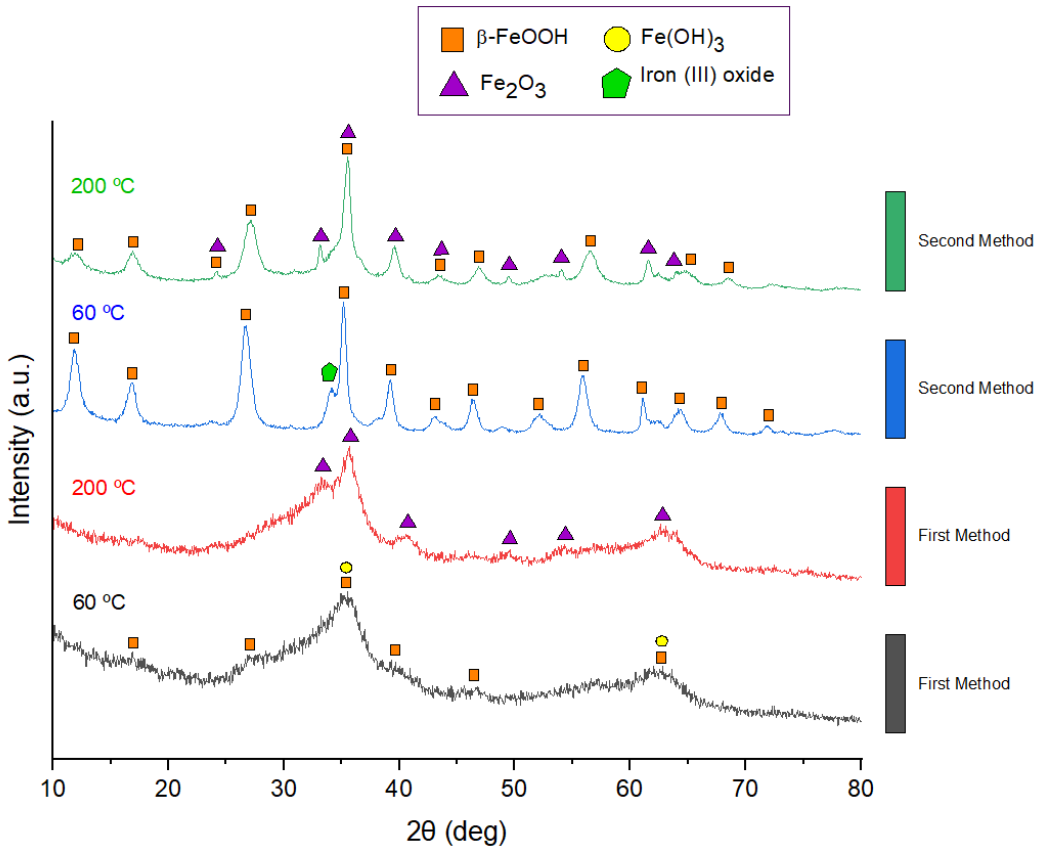

Figure 29: XRD diffractograms of the two synthesis methods perform and associated temperatures attempted for the synthetic β-FeOOH powders.

Figure 30 shows the XRD diffractograms of the synthetic β-FeOOH powder obtained by the previous selected method, the NR and Fe_2O_3. β-FeOOH and NR powders showed similar diffractograms, confirming the presence of β-FeOOH as the main phase. The only difference was found in the presence of a minor phase of iron(III) oxide composition with ammonia in synthetic β-FeOOH powder. Both synthetic and NR compositions reveal broad peaks suggesting the presence of amorphous phases. However, the similarities between the synthetic β-FeOOH composition and the NR allow one to conclude that the synthetic composition obtained is a plausible candidate as the iron oxide feedstock for the electrowinning process.

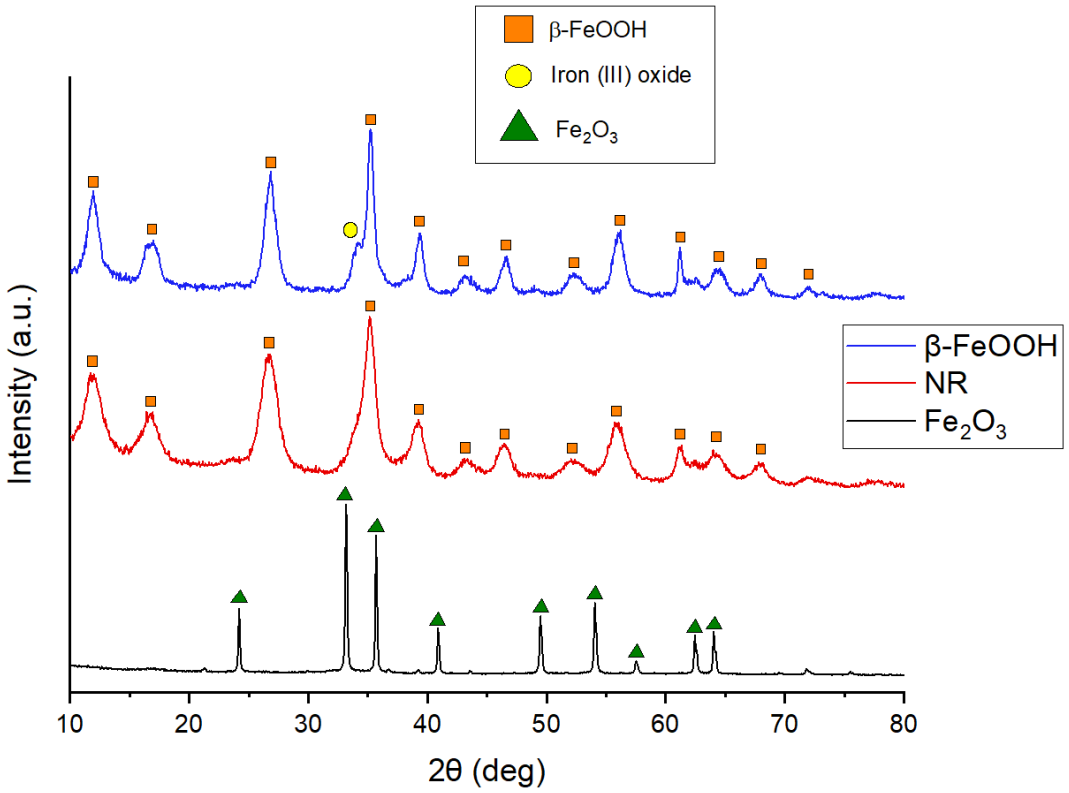

Figure 30: XRD diffractograms of Fe_2O_3, NR and β-FeOOH.

3.1.3. XRF analysis

The XRF analysis of the synthetic β-FeOOH and the NR are shown in the Table 3. Both materials are characterized in its majority with Fe (≥88 wt%). Moreover, the presence of Cl was also found in both cases with around ~9 wt% and ~5 wt% for the synthetic and NR, respectively, as well as low content of oxygen (~1 wt%). These results are in agreement with the XRD results, which main phase consist in of β-FeOOH for both samples.

Lower elements content (< 0.62 wt%) such as Ni, S, P, Ca, Cr. Zn, Co, Mn and Pb are also present in the synthetic β-FeOOH composition and in the NR. However, Ni and S contents are present in relatively higher amount in the NR case (~1.1 and 1.2 wt%, respectively) due to the industrial process where the residue was originated. Nevertheless, their presence it is not expected to have any interference during the alkaline electrolysis to Fe.

Table 3: Elemental XRF analysis (wt%) of β-FeOOH and NR

β-FeOOH (%)	Element	NR (%)
88.2	**Fe**	91.5
8.98	**Cl**	4.50
1.04	**O**	0.85
0.08	**Ni**	1.21
0.01	**S**	1.13
0.22	**P**	0.19
0.15	**Ca**	0.11
0.17	**Cr**	0.02
0.21	**Zn**	0.01
-	**Co**	0.20
0.64	**Mn**	-
0.25	**Pb**	-

3.2. Cyclic voltammetry analysis

Figure 31 shows the CVs recorded at 10 $mV.s^{-1}$ for the suspensions at 90ºC with [NaOH] = 10 M and 100 g/L (iron oxide), where one can correlate the redox reactions that occur during electrolysis in all studied cases. The plots show the current density ($A.cm^{-2}$) as a function of potential (V). The marked "C" peak corresponds to the cathodic reactions, which is associated with reduction process.

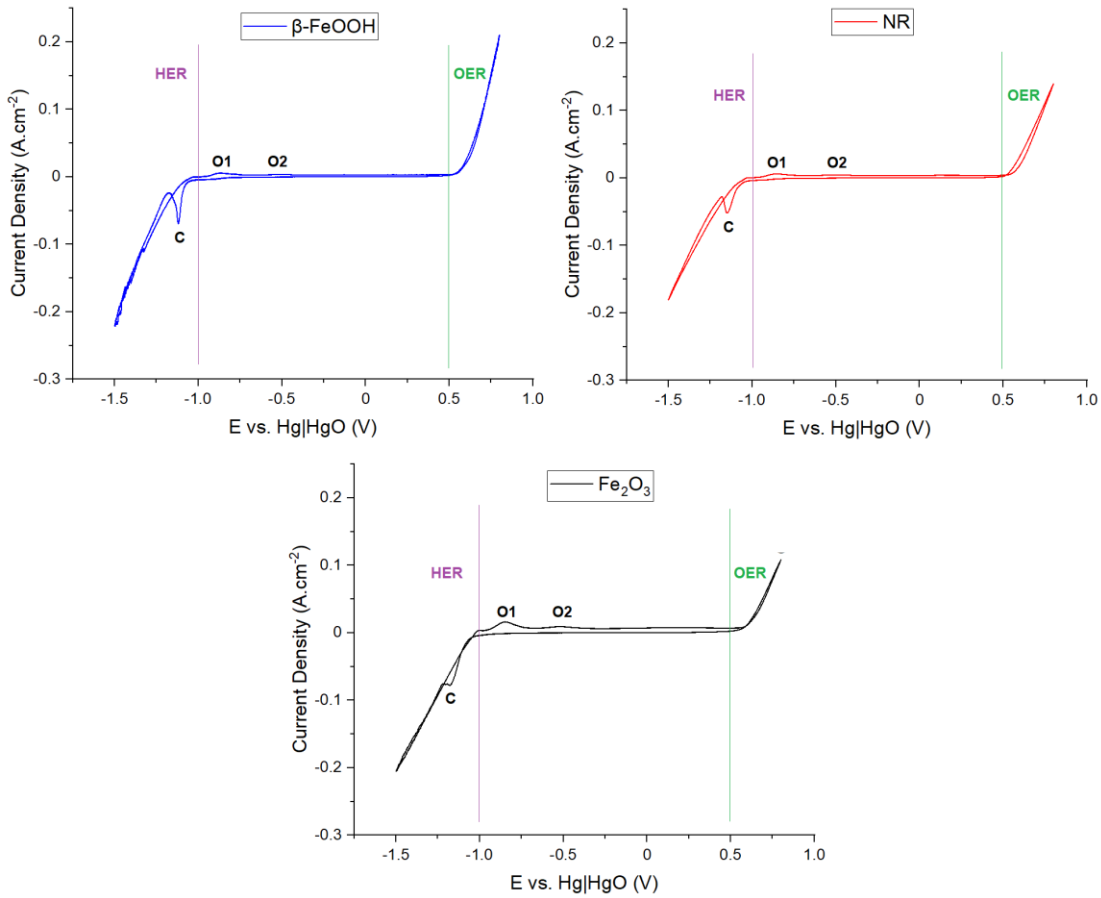

Figure 31: Cyclic voltammetry of β-FeOOH, NR and Fe_2O_3, respectively, at 90°C with [NaOH] = 10 M and 100 g/L (iron oxide).

The associated redox peaks are related to following, in agreement with Pourbaix diagrams and literature [10, 26, 32].

- C – Cathodic peak from the reduction of Fe(III and II) aqueous species into Fe at -1.15 V approximately;
- HER – Hydrogen Evolution Reaction at starting on the onset potential of ~ -1.0 V to cathodic polarizations;
- O1 – Oxidation of Fe to Fe(II) aqueous species at -0.8V.
- O2 – Oxidation of Fe(II) aq. Species to Fe(III) at -0.5 V.
- OER – Oxygen Evolution Reaction starting from ~ 0.5 V to more anodic polarizations.

O1 species are typically $Fe(OH)_3^-$ and $HFeO_2^-$, while O2 are associated with FeOOH and/or Fe_3O_4 [10, 25, 31]. HER and OER are due to the water splitting in alkaline medium occurring at the cathode, as HER and at the anode, as OER. Both reactions are demonstrated in chemical reactions (18) and (19).

$$2H_2O + 2e^- \rightarrow H_2(g) + 2OH^- \quad (18)$$

$$4OH^- \rightarrow O_2(g) + 4e^- + 2H_2O \quad (19)$$

The cathodic peak (C) of reduction to Fe is superimposed to HER region, as expected from the literature analysis in the present Thesis [9, 10, 17, 24, 34, 37]. Since H_2 competes with Fe for the cathodic current, one expects a decrease of the Faradaic efficiency of the deposition process. During reduction of the iron hydroxides and/or oxides, the Fe(III) particles in the vicinity of the cathode suffer dissolution to Fe(III) aqueous species and are reduced to Fe(II) aqueous species. Consequently, Fe(II) in the aqueous solution will be reduced and deposited as Fe^0 on the cathode.

3.3. Galvanostatic Deposition

3.3.1. Comparation of different materials and their efficiencies

Figure 32 shows chrono potentiometry from galvanostatic depositions of 100 g/L of β-FeOOH, Fe_2O_3 and NR suspensions and 50 g/L of β-FeOOH with [NaOH] = 10 M, at 90 ºC and -0.025 A.cm^{-2}. Two different loads of β-FeOOH were used due to some difficulties encountered in the deposition when higher Fe loads were tried. It was observed a very viscous electrolyte in the first few hours of the deposition, resulting in very low Faradaic efficiency of the β-FeOOH particles reduction to Fe ($\eta_{faradaic}$ = 4%) and high background noise. The high viscosity restricted the free movement of the suspended particles being unable to reach and then to be reduced at the cathode. Many approaches were investigated, such as increasing the rotation speed of the magnet stirring, reduction of the ammonia in the synthesis and vacuuming the electrolyte after the synthesis to expel gases that could cause this problem. One should also note that a similar behavior of high viscosity was faced by Feynerol at al. when using α-FeOOH as feedstock for the electrochemical cell [18]. Nevertheless, none of the tried approaches were successful. Two plausible explanations for this can be i) the presence of iron (III) oxide composition with ammonia (seen in chapter 3.1.2) which might lead to some precipitate formation, increasing the viscosity, or most likely to ii) the highly cohesive interactions between the β-FeOOH particles are somehow unfavorable to the evolution of O_2 bubbles due to their larger size in comparison with the O_2 bubbles as registered by Feynerol. To counteract this problem, the load of β-FeOOH in the electrolyte was reduced to half. The problem of the high viscosity was solved, and the electrolyte remained liquid through the 4 hours of deposition. Also, the background noise disappeared, and the current reached higher cathodic values. However, it was not enough to significantly increase the Faradaic efficiency and just a 2% increment was achieved. When decreasing the β-FeOOH load available in suspension, one it is also decreasing the amount of iron oxide available to be reduced to Fe. Thus, a considerable decrease of the iron mass as deposit is expected to be lower, which might be the reason affecting the Faradaic efficiency to such low levels.

The first 16 h galvanostatic depositions of Fe_2O_3 and NR suspensions were conducted at 90 ºC with 10 M NaOH solutions for comparison purposes with the results obtained with the synthetic composition. Both materials reached similar potential (V) level at the end of the deposition however, the behavior of each curve is slightly different.

For the NR curve the potential was found to be faster stabilized, with no major variations after 2 hours of deposition. Meanwhile, it took about 8 hours for the Fe_2O_3 case to reach a constant potential, due to the occurrence of two peak oscillations at 6 and 8 hours, explained by the loss or disintegration of some Fe deposit at the cathode. This explains the lower efficiency obtained regarding the deposition from NR. During NR deposition, the potential plot shows a more stable behavior, resulting in a Faradaic efficiency of 59%. Deposition from Fe_2O_3 suspensions in the same conditions shows an efficiency of 57%, as exhibited in Table 4.

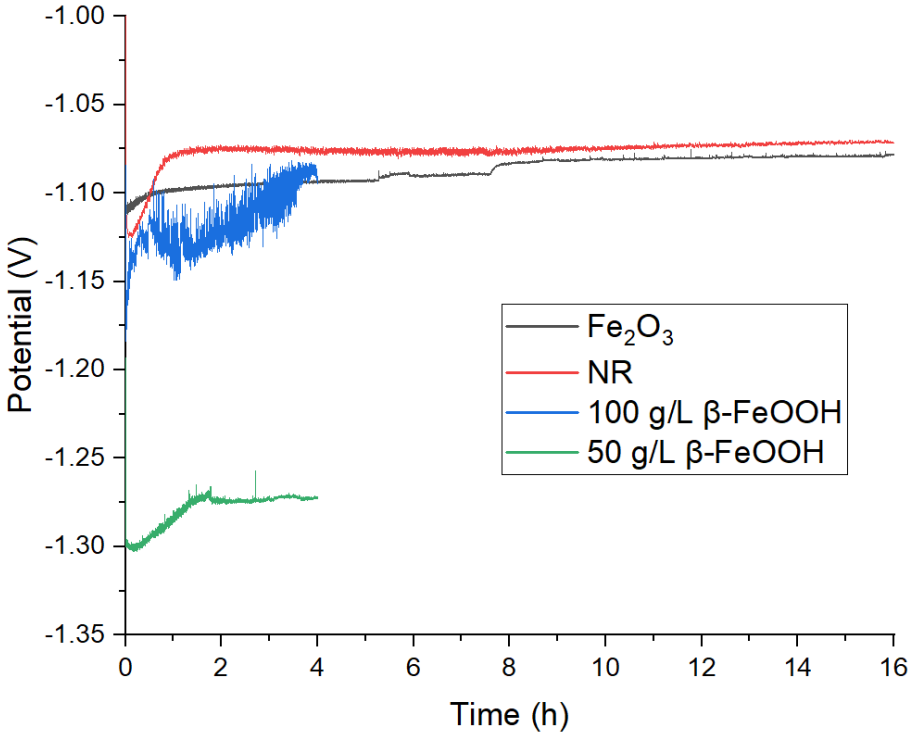

Figure 32: Chrono potentiometry from galvanostatic depositions of 100 and 50 g/L of β-FeOOH and 100g/L of Fe_2O_3 and NR suspensions with [NaOH] = 10 M, at 90 ºC and -0.025 A.cm^{-2}.

The chrono potentiometry from galvanostatic depositions of 100 g/L of Fe_2O_3 and NR suspensions were studied at 105, 120 and 130 ºC and 18 M NaOH aqueous solutions for 16 hours. The increase of the NaOH concentration from 10 to 18 M at temperatures ≥105 ºC is due to the fast evaporation of the aqueous NaOH solution inside of the electrochemical cell. Thus, the use of a more concentrated salt electrolyte (18 M) prevents the evaporation and allow one to also study the impact of the electrolyte concentration simultaneously. The chronopotentiometry are shown in Figure 33.

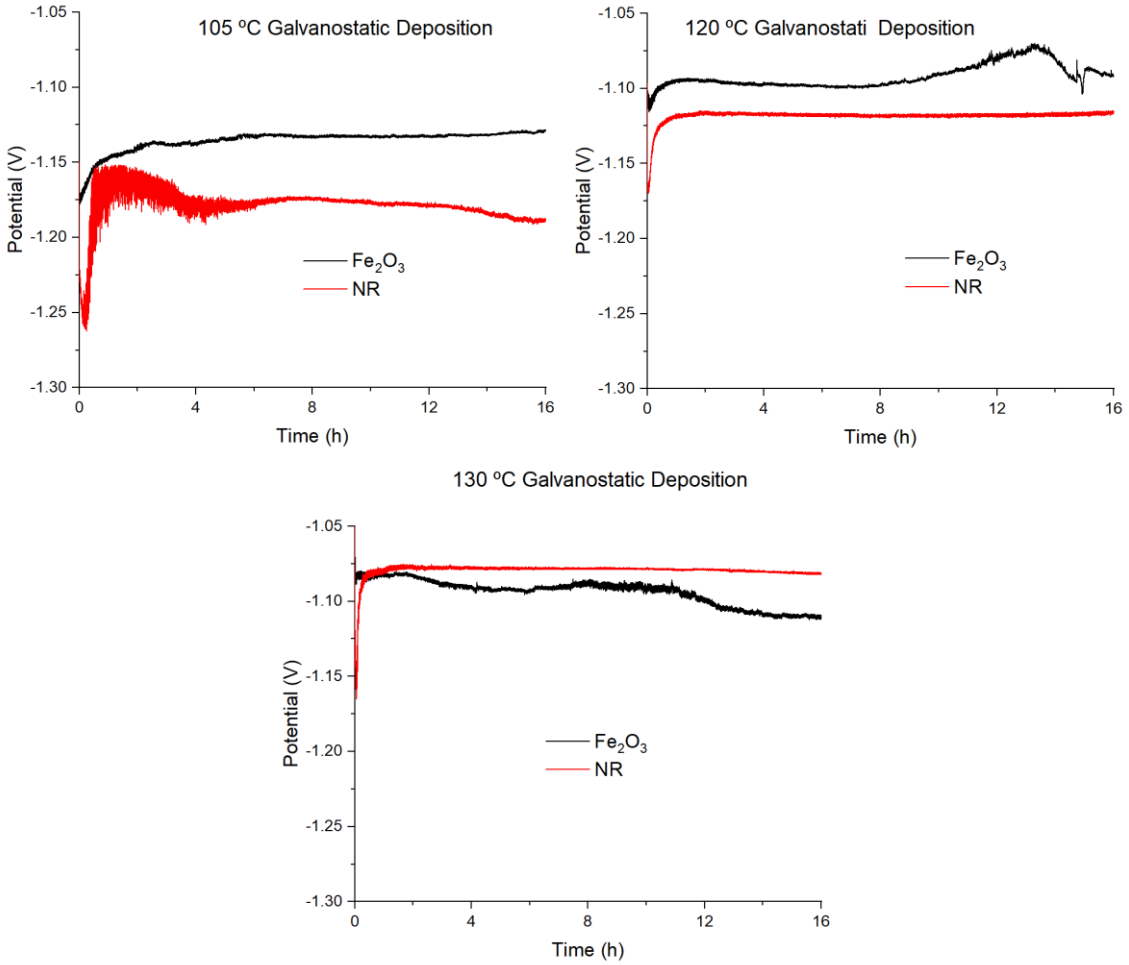

Figure 33: Chrono potentiometry from galvanostatic depositions of 100g/L of Fe2O3 and NR suspensions at 105, 120 and 130 ºC with [NaOH] = 18 M, for 16 hours.

At 105 ºC with an 18 M NaOH electrolyte, the NR deposition started with high background noise, only being able to stabilize its potential after 7 hours, which compromised the deposition of Fe, meaning that the first Fe layers deposited at the cathode were soon found very weak and mechanically unstable. Later, with the use of an ultrasonic bath for cleaning the NaOH from the deposits surface, the Fe deposit was lost (Figure 34), explaining the extremely low Faradaic efficiency of 0.5%. For Fe_2O_3, the deposition was found to be more stable with less oscillation of the potential resulting in an 84% of Faradaic efficiency (Table 4).

At 120 ºC both depositions initiated at a very stable rate, however the Fe_2O_3 suspension showed several fluctuations are visible in the final hours and ended at a similar potential. Fe_2O_3 demonstrated once again higher Faradaic efficiency of 69% against the 40% of NR (Table 4). This stabilization of potential is supposed to give a high adhesion to the Fe deposited with NR particles.

Finally, during the Fe deposition from the NR suspension at 130 ºC, the potential stabilized very quickly reaching 21% of Faradaic efficiency. Fe_2O_3 showed a potential tending to more cathodic values reaching a higher Faradaic efficiency of 48.1% (Table 4).

The behavior is similar for Fe_2O_3 and NR suspensions, one can see that the 90 ºC depositions shows lower cathodic potentials. Moreover, generally with the rise of the temperature for the suspensions with 18 M NaOH concentration, the potential is increasingly anodic. This might be explained by the decline of the H_2 evolution with the rise of the temperature. Another similar behavior in all the chronopotentiometry plots can be observed resulting in the initial sudden decrease of the potential (V) at the initial phase of reduction, due to possibly to the reduction of an oxidized layer on the steel substrate [16].

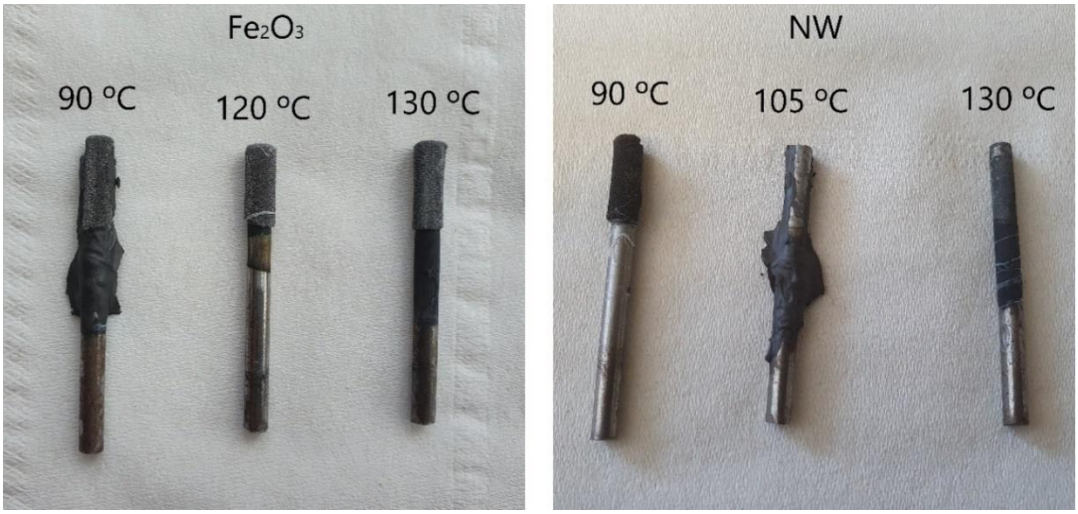

Figure 34: Cathodes after the galvanostatic deposition of 100 g/L of Fe_2O_3 and NR suspensions, respectively.

Table 4: Deposited mass (g) in the cathode and the Faradaic efficiency (%) achieved from the galvanostatic depositions of NR (orange) and Fe2O3 (green) suspensions at 90 with [NaOH] = 10 M, and at 105, 120 and 130 ºC with [NaOH] = 18 M for 16 hours.

Temperature (ºC)	[NaOH] (M)	Deposited mass (g)	$\eta_{Faradaic}$ (%)
90	10	0.165	59.3
		0.158	57
105	18	0.0014	0.504
		0.233	83.8
120		0.111	39.8
		0.191	68.9
130		0.058	21.0
		0.133	48.1

3.3.2. Microstructures from SEM and EDS images

Figure 35, Figure 36 and Figure 37 show the SEM images of the Fe deposits obtained from the electrodeposition of β-FeOOH, Fe_2O_3 and NR powder suspensions at 90 ºC. The Fe microstructures of the β-FeOOH suspensions show a heterogeneous structure in comparison with the remaining feedstocks. Moreover, the Fe deposits not only seems to be smaller but more widely spaced when compared with the other compositions tried as suspensions. This can be associated with the low mechanical strength of the deposits when the synthetic composition was used as feedstock. On the other hand, NR and Fe_2O_3 show Fe deposits similar to dendritic crystals in fair agreement with literature [22, 28, 29].

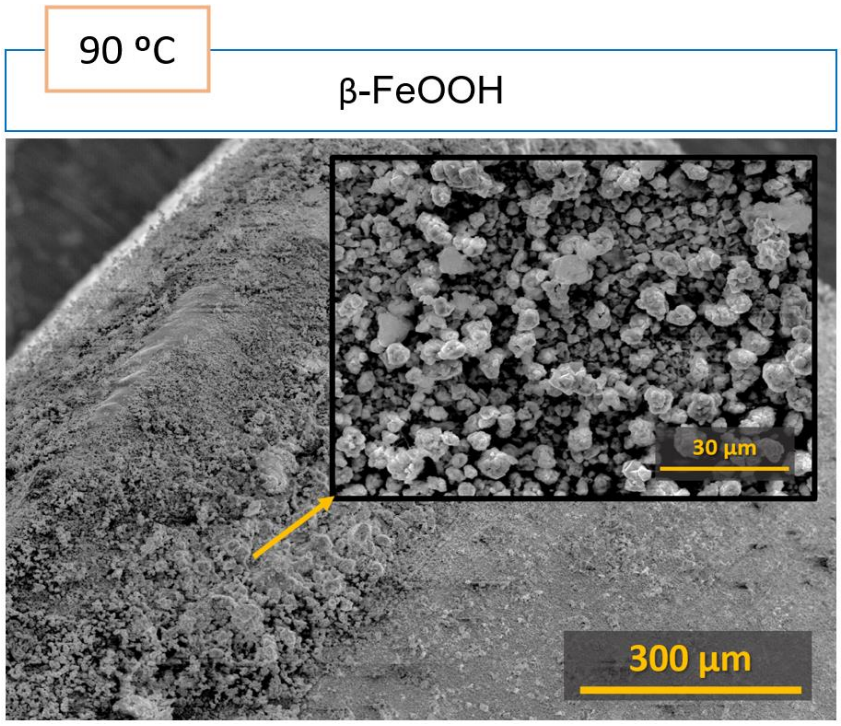

Figure 35: SEM images of the Fe galvanostatic deposition from 100 g/L of β-FeOOH suspension at 90 ºC, with [NaOH] = 10 M and -0.025 A.cm^{-2}.

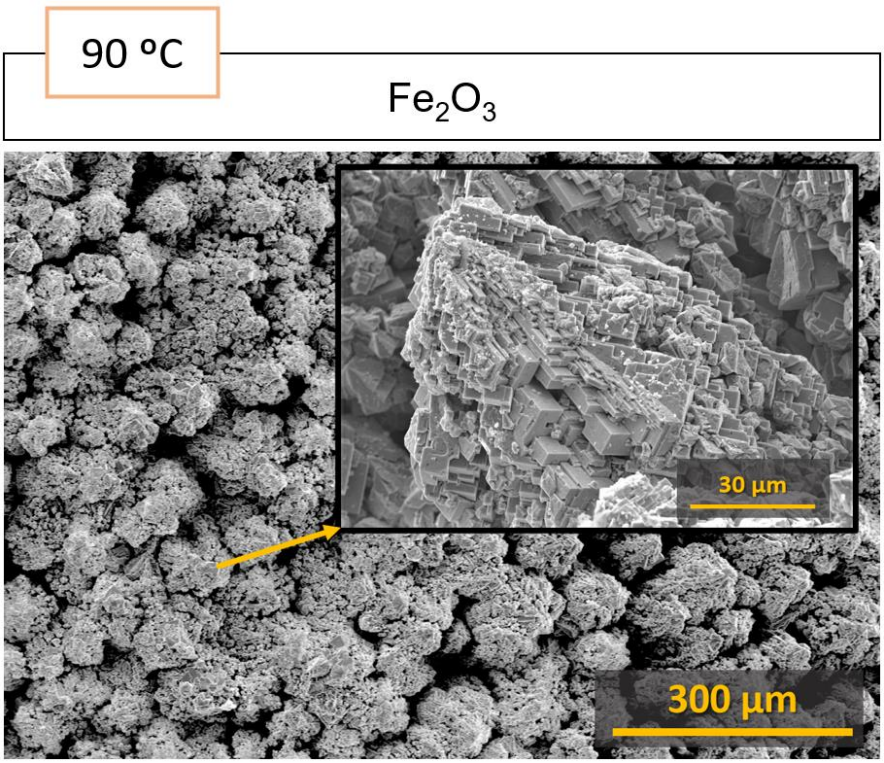

Figure 36: SEM images of the Fe galvanostatic deposition from 100g/L of Fe_2O_3 suspension at 90 ºC with [NaOH] = 10 M and -0.025 A.cm^{-2}.

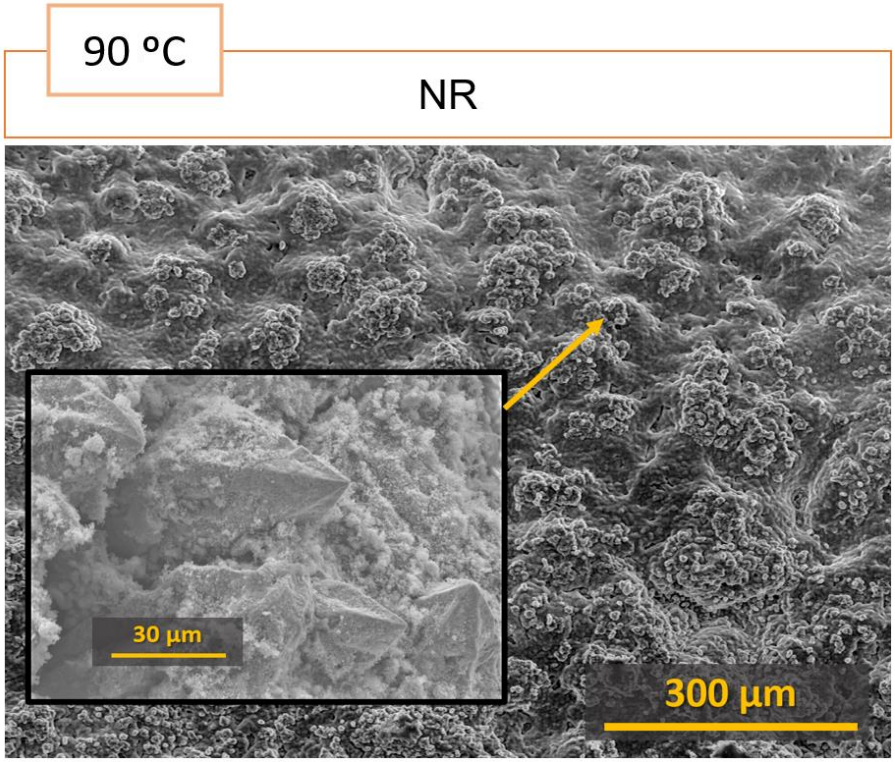

Figure 37: SEM images of the Fe galvanostatic deposition from 100 g/L of NR suspension at 90 ºC with [NaOH] = 10 M and -0.025 A.cm^{-2}.

Figure 38 shows the EDS images of the Fe deposits obtained from the electrodeposition of Fe_2O_3 and NR powder suspensions at 90 ºC. It is clear the presence of Fe (marked at red in the EDS mapping) in the microstructures. A covering layer of NaOH from the electrolyte (marked at yellow at the EDS mapping image) can be seen in the case of the NR, also trapped between the Fe dendrites. This issue was improved when the Fe_2O_3 was used as suspension due to the use of the ultrasonic bath for a proper cleaning of the Fe deposits. Nevertheless, the Fe deposits are visible in both cases and have similar dendritic shape as the ones obtained with the Fe_2O_3 suspensions.

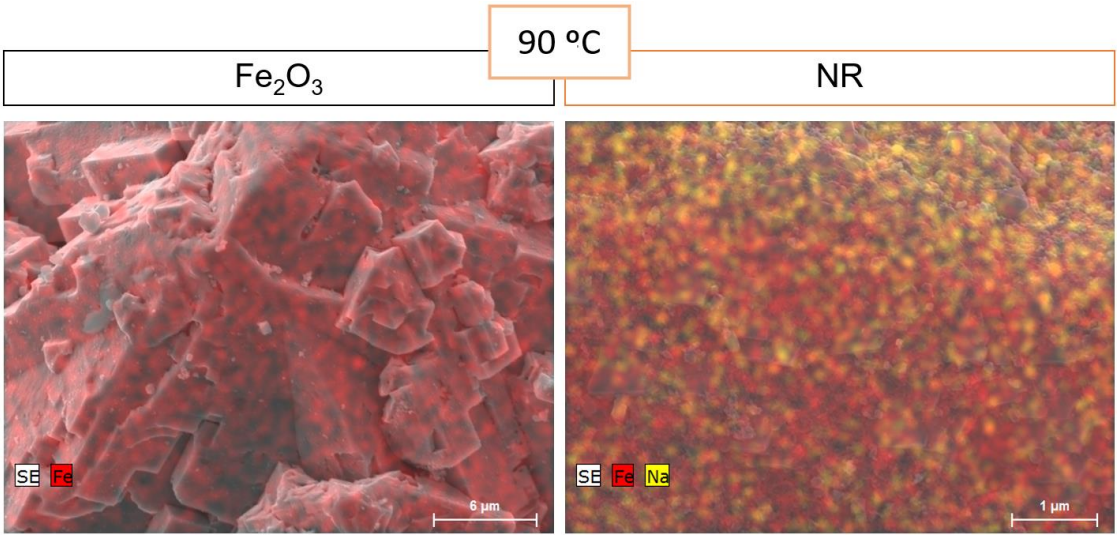

Figure 38: EDS images of the Fe galvanostatic deposition from Fe_2O_3 and NR at 90 ºC with [NaOH] = 10 M and -0.025 A.cm^{-2}, respectively.

Images for the deposits obtained at the higher temperatures (105, 120 and 130 ºC from Fe_2O_3 and NR suspensions) are shown from Figure 39 to Figure 44. At 105 ºC, the deposits show smaller Fe clusters for the reasons explained by the high background noise shown in the respective chrono-potentiometry (Figure 33), which compromised the deposition of Fe, meaning that the first iron layers deposited at the cathode were very weak and mechanically unstable. The depositions of Fe at 120 and 130 ºC from NR and Fe_2O_3 suspensions it is perfectly seen the Fe clusters agglomerated at the cathode surface. With the increase of temperature, the amount of iron deposited decreases as well as the Faradaic efficiencies. Overall, Fe_2O_3 suspensions demonstrated a higher level of Fe depositions than NR. At 120 ºC for the Fe deposition from NR suspensions and at 105 ºC from Fe_2O_3 suspensions, one can see the Fe grains shaped by nodules stacked on top of one another, creating dendrites.

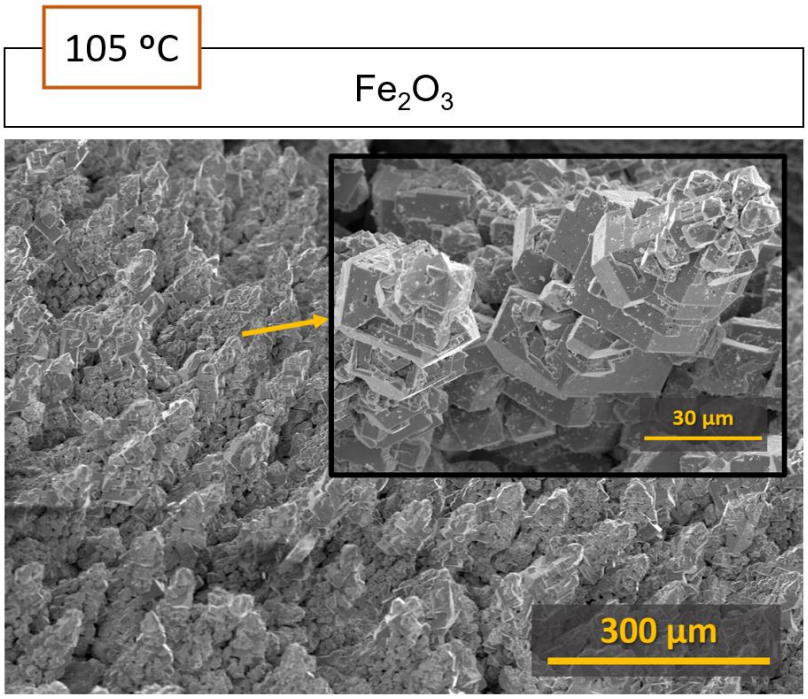

Figure 39: SEM images of the Fe galvanostatic deposition from 100g/L of Fe_2O_3 suspension at 105 °C with [NaOH] = 18 M and -0.025 A.cm^{-2}.

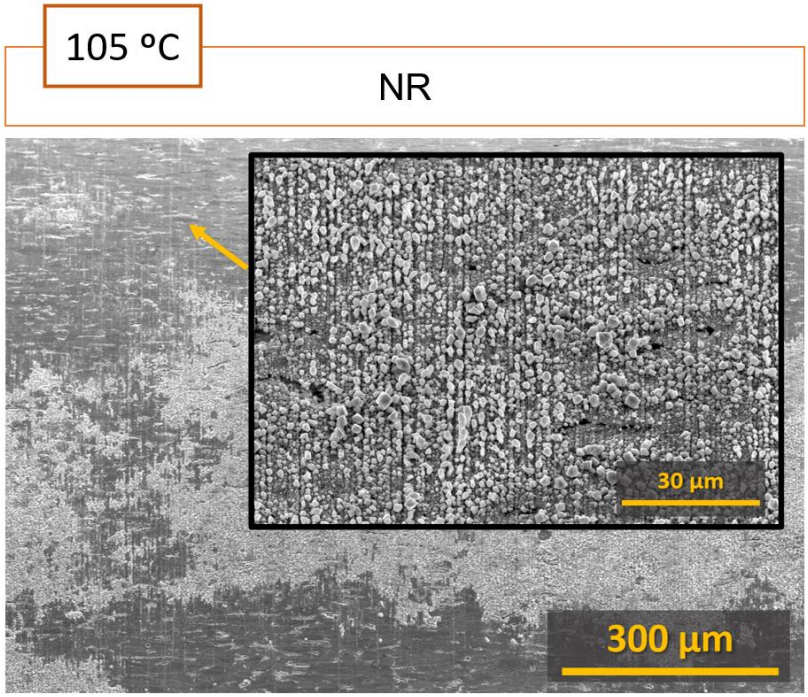

Figure 40: SEM images of the Fe galvanostatic deposition from 100 g/L of NR suspension at 105 °C with [NaOH] = 18 M and -0.025 A.cm^{-2}.

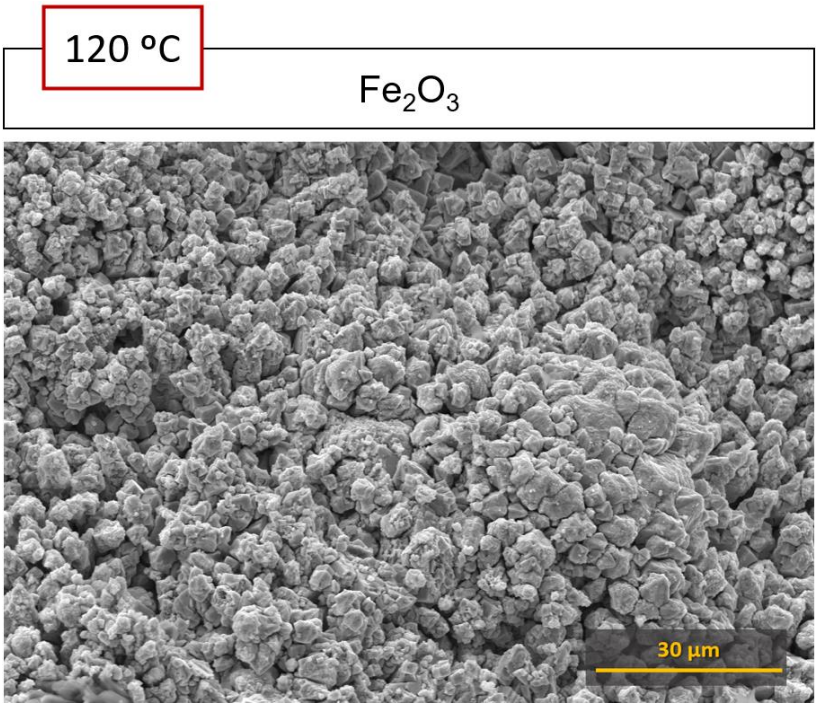

Figure 41: SEM images of the Fe galvanostatic deposition from 100 g/L of Fe_2O_3 suspension at 120 °C with [NaOH] = 18 M and -0.025 A.cm^{-2}.

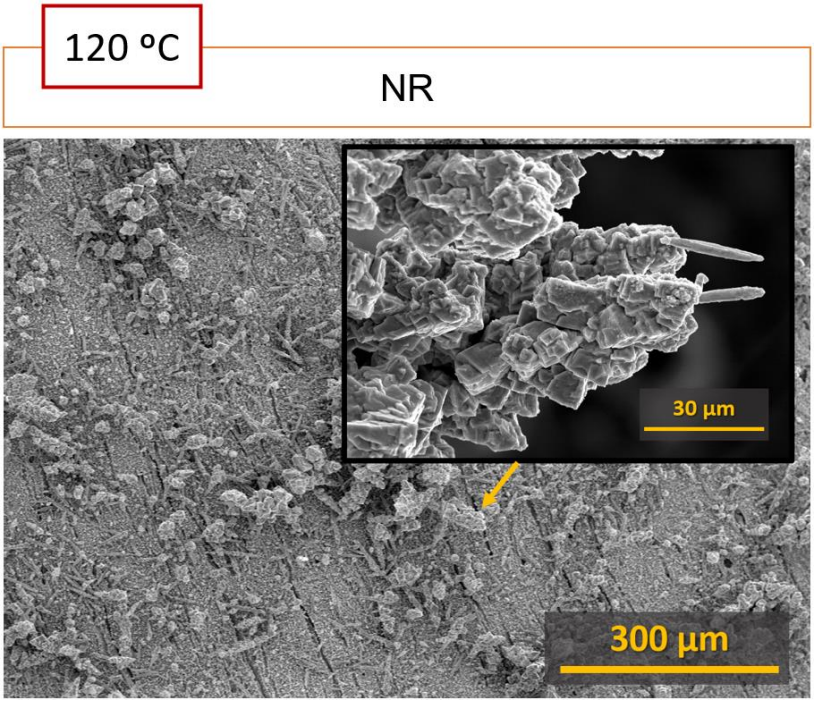

Figure 42: SEM images of the Fe galvanostatic deposition from 100 g/L of NR suspension at 120 °C with [NaOH] = 18 M and -0.025 A.cm^{-2}.

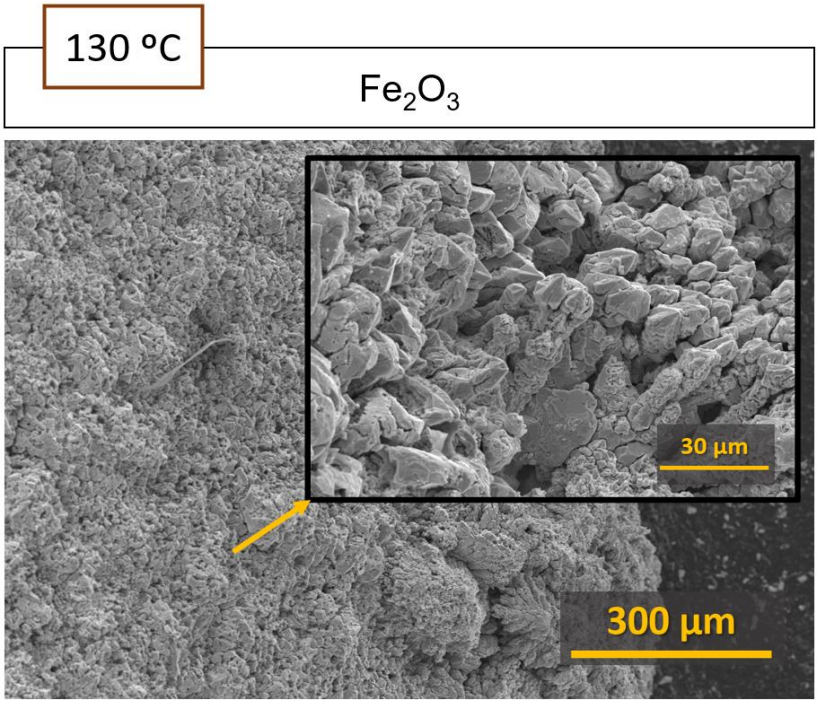

Figure 43: SEM images of the Fe galvanostatic deposition from 100 g/L of Fe_2O_3 suspension at 130 °C with [NaOH] = 18 M and -0.025 A.cm^{-2}.

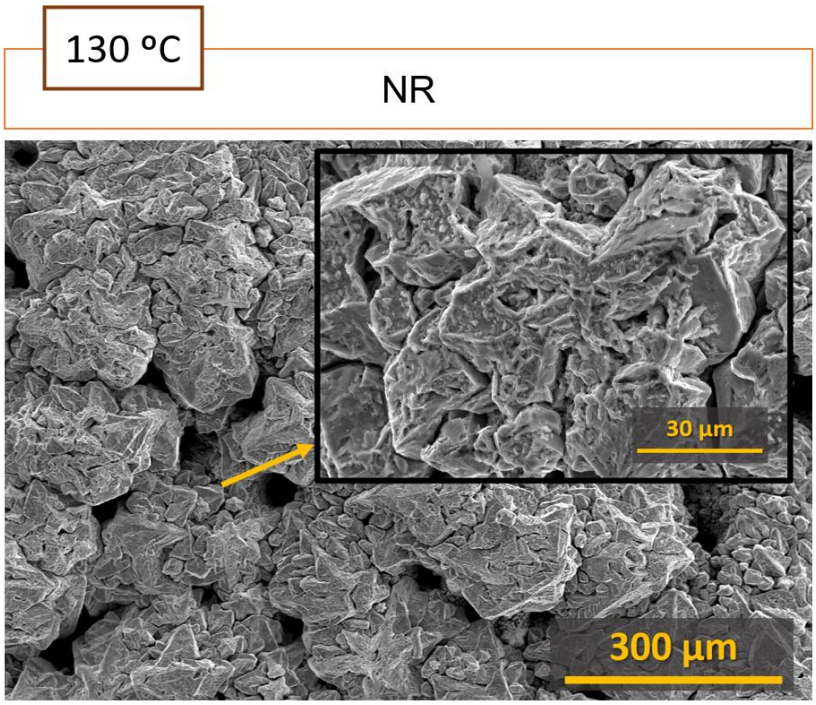

Figure 44: SEM images of the Fe galvanostatic deposition from 100 g/L of NR suspension at 130 °C with [NaOH] = 18 M and -0.025 A.cm^{-2}.

The Fe_2O_3 suspensions formed homogeneous and compacted Fe deposits at all temperatures, as confirmed by the EDS mapping image (Figure 45). It is clear, once again, the presence of Fe (marked at red in the EDS mapping) in the microstructure and similar dendritic shape as the ones obtained at other temperatures from Fe_2O_3 and NR

suspensions. The use of the ultrasonic bath for a proper cleaning of the Fe deposits was successful in this instance.

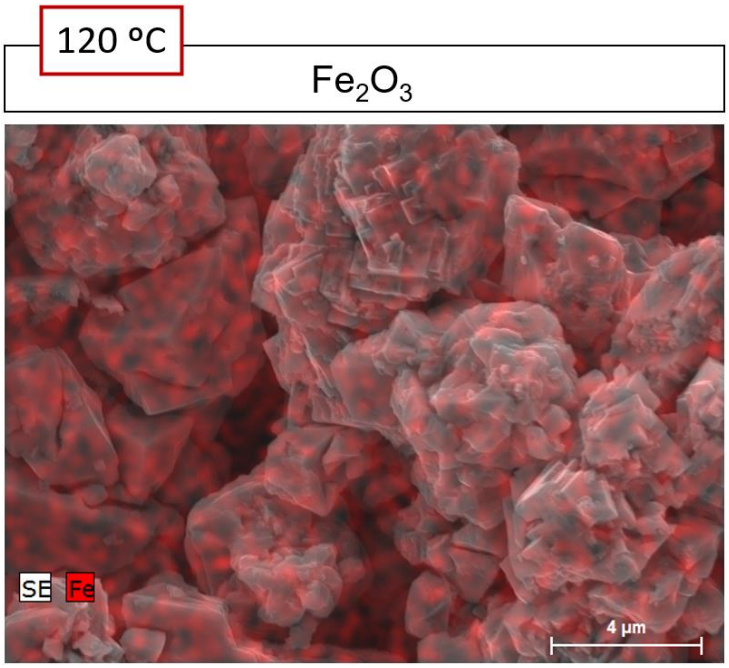

Figure 45: EDS image of the Fe galvanostatic deposition from 100 g/L of Fe_2O_3 suspension at 120 °C with [NaOH] = 18 M and -0.025 A.cm^{-2}.

3.3.3. Phase identification of the deposits

The XRD diffractogram of the deposits obtained by galvanostatic deposition at 90, 105, 120 and 130 ºC are shown in Figure 46 and Figure 47 . XRD diffractograms confirmed that Fe is the main phase. The only impurity, Fe_3O_4 is due to the oxidation of Fe deposits. One can conclude that the galvanostatic mode from Fe_2O_3 and NR suspensions at higher temperatures and with 18 M NaOH electrolyte were successful at depositing Fe at the cathode.

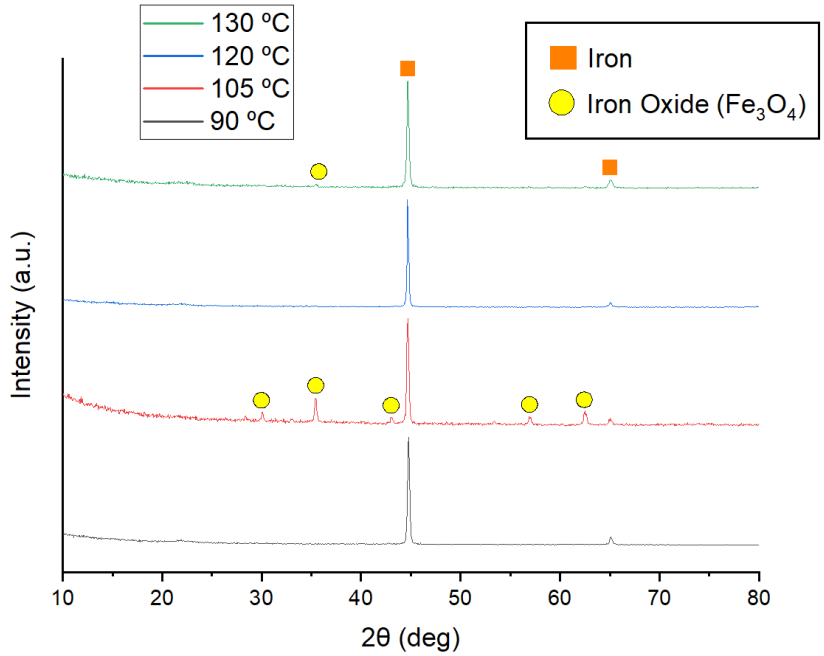

Figure 46: XRD diffractogram of the Fe deposits from the galvanostatic deposition at 90 ([NaOH] = 10 M), 105, 120 and 130 ºC ([NaOH] = 18 M) from 100 g/L of Fe_2O_3 suspensions with -0.025 A.cm^{-2}.

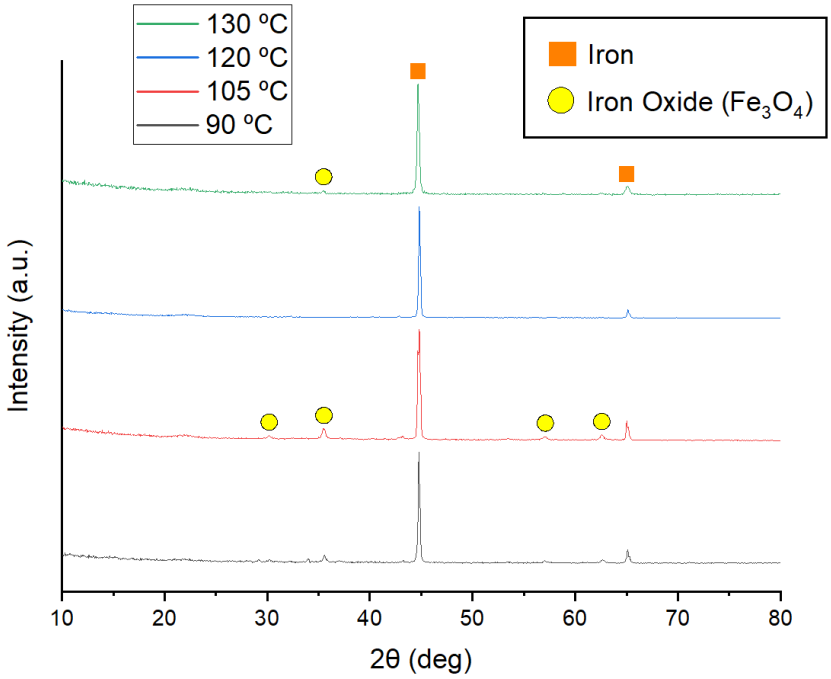

Figure 47: XRD diffractogram of the Fe deposits from the galvanostatic deposition at 90 ([NaOH] = 10 M), 105, 120 and 130 ºC ([NaOH] = 18 M) from 100 g/L of NR suspensions with -0.025 A.cm^{-2}.

3.4. Potentiostatic Deposition

3.4.1. NR depositions and efficiencies

The chronoamperometric study of the electrodeposition from 100 g/L of NR suspensions is shown in Figure 48, at -1.075, -1.10 and -1.15 V for 16 hours at 90 ºC with [NaOH] = 10 M. The potentiostatic studies (fixed potential) were based on the potential of the cathodic peak obtained during the cyclic voltammetry analysis (chapter 3.2). The plots show the current density ($A.cm^{-2}$) as a function of time (hours) and allow one to study the impact of the potential choice with the Faradaic efficiency. Thus, the limiting factors affecting can be studied in detail. Potential optimization plays an important role in the electrochemical processes transition to galvanostatic mode, considering industrial needs, such as energy costs, such as the optimal potential and deposition time [35].

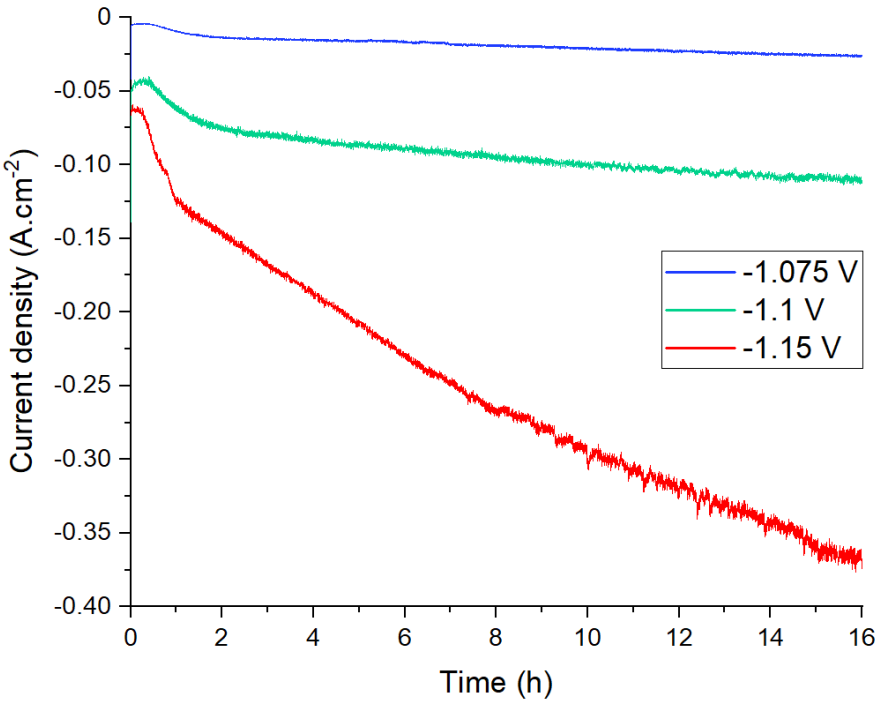

Figure 48: Chrono amperometry plots of potentiostatic Fe deposition from 100 g/L of NR suspensions at -1.075, -1.10 and -1.15 V for 16 hours, at 90 ºC with [NaOH] = 10 M.

The deposition features higher current densities when increasing the cathodic polarizations, showing higher Fe deposited mass. The increase of the current density at -1.15 V leads to a more viscous electrolyte formation, without compromising the deposition as in the synthetic composition's case. However, Fe deposits were found attached on the magnetic stirrer (Figure 49) at -1.15 V cathodic experimental conditions. The viscosity of the suspension during stirring most likely jeopardizes the Fe deposition on the cathode, since some of it ends being collected on the magnetic stirrer by diffusion issues. On the other hand, at -1.075 V the formation of Fe deposits is low due to the insufficient cathodic potential.

Figure 49: Fe caught by the magnetic stirrer at -1.15 V during the deposition.

Table 5 shows the deposited mass (g) of the electrodes and the associated Faradaic efficiency (%) achieved from NR suspensions at -1.075, -1.10 and -1.15 V. The three depositions show high values of Faradaic efficiencies. However, very different Fe deposits weight were obtained (Figure 50). The similarity of the Faradaic efficiencies with the very different Fe deposited is due to the current density applied in each case. With less than 10% of efficiency difference between all the cases, HER seems to not have a strong impact in these specific potentials applied. The same case would not occur for higher cathodic polarizations as studied in [64].

Table 5: Deposited mass (g) in the electrode and the Faradaic efficiency (%) achieved from 100 g/L of NR suspensions at -1.075, -1.10 and -1.15 V for 16 hours, at 90 ºC with [NaOH] = 10 M.

Voltage (V)	Deposited mass (g)	$\eta_{Faradaic}$ (%)
-1.075	0.189	91
-1.10	0.835	82
-1.15	2.319	83

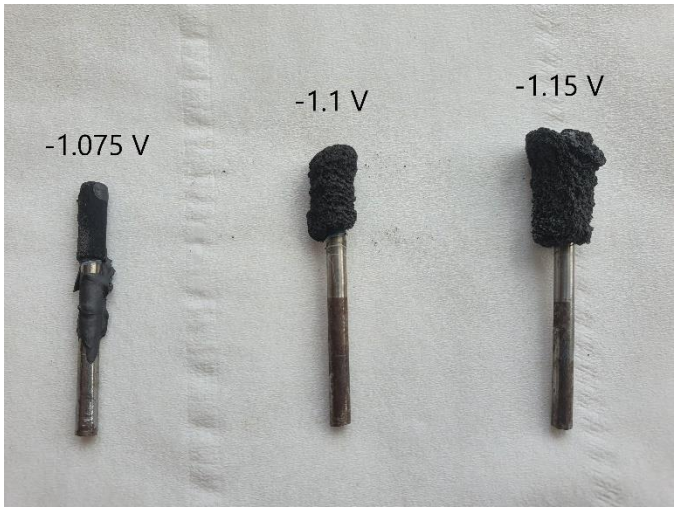

Figure 50: Cathodes after 16 hours Fe potentiostatic deposition from 100 g/L of NR suspensions at -1.075, -1.10 and -1.15 V, at 90 ºC with [NaOH] = 10 M, respectively.

3.4.2. SEM and EDS images

SEM images of Fe deposits obtained at the different cathodic polarizations of -1.075, -1.10 and -1.15 V from the NR suspensions are shown in Figure 51, Figure 52 and Figure 53. In all cases, the growth of Fe dendrites is visible, also observed in Figure 54. The microstructures obtained at -1.075 V show smaller dendrites covered, most likely, with NaOH. In fact, a low deposited Fe mass was obtained in this case, which can be explained due to the insufficient cathodic polarization applied. The sample obtained with -1.10 V shows higher Fe dendrites and the presence of a thin layer of sodium slats was validated by the XRD diffractogram in Figure 55 and by the EDS images in Figure 54. The Fe microstructures obtained on the sample deposited at -1.15 V show the biggest and sharpest dendrites, due to the high mass deposited on the cathode.

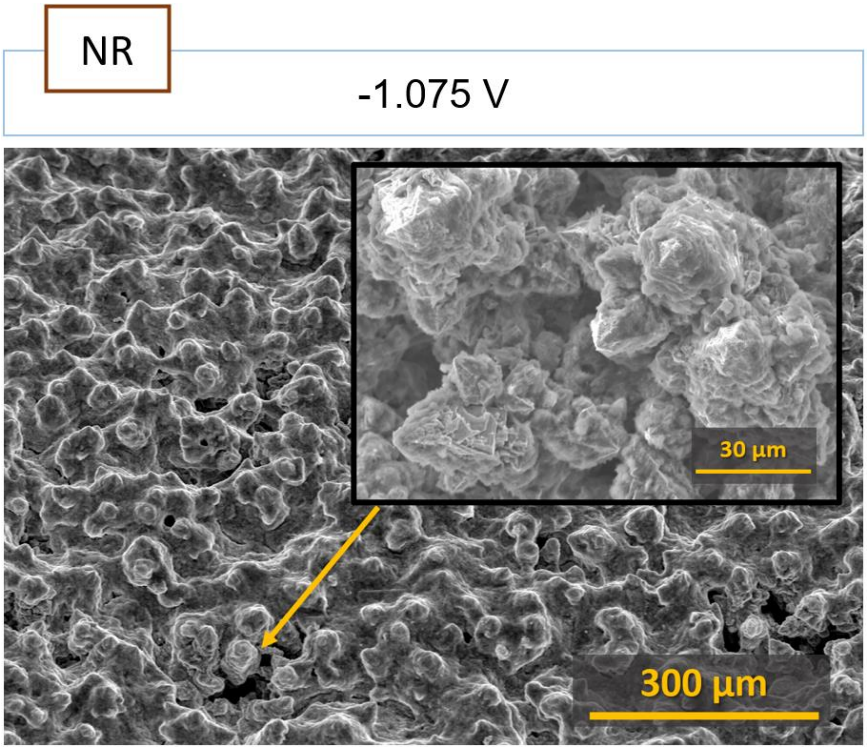

Figure 51: SEM images of the Fe deposits obtained by potentiostatic deposition at -1.075 V from 100 g/L of NR suspension, at 90 ºC with [NaOH] = 10 M for 16 hours.

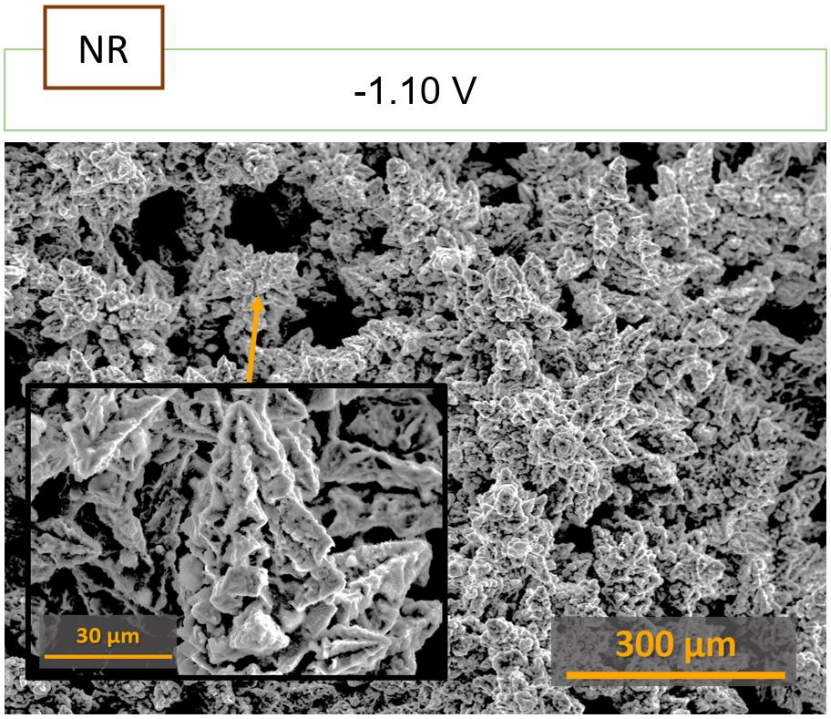

Figure 52: SEM images of the Fe deposits obtained by potentiostatic deposition at -1.10 V from 100 g/L of NR suspension, at 90 ºC with [NaOH] = 10 M for 16 hours.

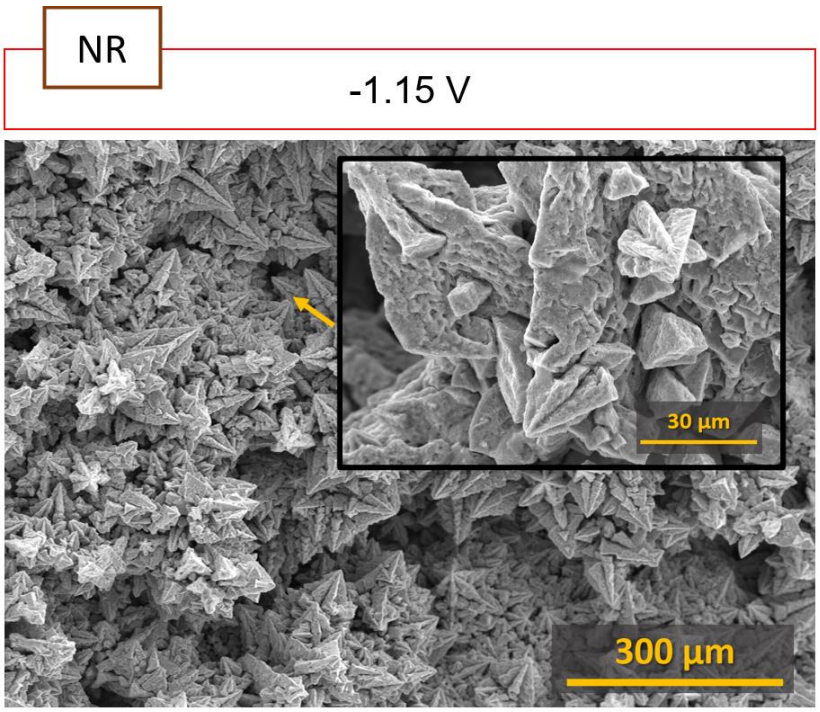

Figure 53: SEM images of the Fe deposits obtained by potentiostatic deposition at -1.15 V from 100 g/L of NR suspension, at 90 ºC with [NaOH] = 10 M for 16 hours.

In Figure 54 it is shown the presence of Fe and Na in the sample obtained by potentiostatic deposition at -1.075 V. The presence of Fe is noticeable in higher proportions at the dendrite. Despite an attempt to minimize the presence of Na salts

(impurity from the electrolyte) from the Fe deposits by using the ultrasonic bath, its presence is frequent in all samples.

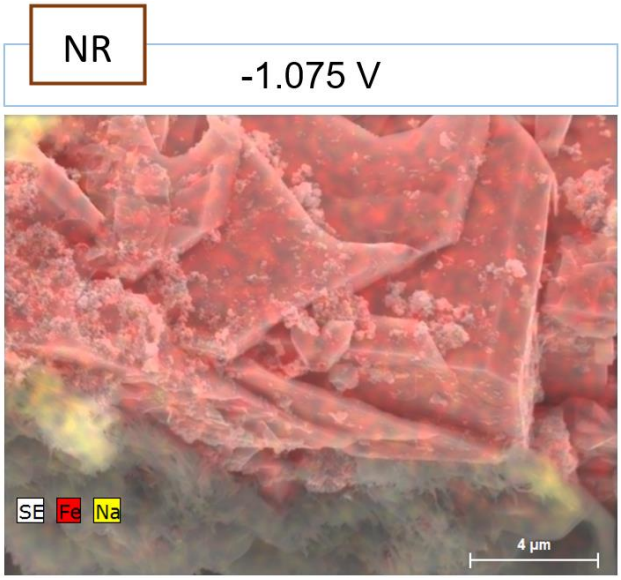

Figure 54: EDS mapping of the Fe deposit at -1.075 V from 100 g/L of NR suspensions, at 90 ºC with [NaOH] = 10 M for 16 hours.

3.4.3. Phase composition of the deposits

The XRD diffractogram of the deposits obtained by potentiostatic deposition at -1.10 and -1.15 V from NR suspensions are shown in Figure 55. XRD diffractograms confirmed that Fe is the main phase. Impurities are also present in a negligible amount due to the electrolyte. The presence of Fe_3O_4 is due to the oxidation of Fe deposits. Thermonatrite ($Na_2CO_3 \cdot H_2O$) is originated by the lack of time in the ultrasonic bath to clean properly the deposit. This led to an excessive amount of NaOH in the deposits, that by reacting with CO_2 formed sodium carbonates.

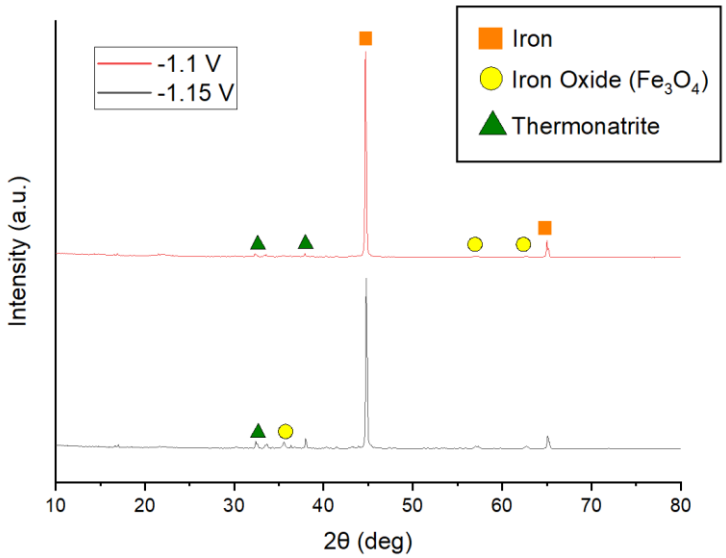

Figure 55: XRD diffractogram of the Fe deposits from the potentiostatic deposition at -1.10 and -1.15 V from 100 g/L of NR suspensions, at 90 ºC with [NaOH] = 10 M for 16 hours.

4. Conclusions

The valorization study of using an industrial iron-rich residue as a feedstock for Fe production seeking future steel manufacturing was accomplished, drawing the following conclusions:

1. Iron deposition is possible when using all synthetic iron oxides compositions (Fe_2O_3 and β-FeOOH) and also with the industrial residue (NR) suspended in a highly concentrated alkaline solution of NaOH at low temperatures, either in galvanostatic or potentiostatic modes.
2. Fe depositions from the synthetic compositions, β-FeOOH, were accessed yet with very low efficiencies due to the high viscosity of the electrolyte. The free movement of the suspended particles and gases (O_2 and H_2) diffusion were restricted leading to lower kinetic rate depositions, revealing lower efficiencies ($\eta_{faradaic}$=4%). Moreover, the presence of iron (III) oxides composition with ammonia might lead also to the formation of agglomerates increasing the viscosity. To counteract this problem, the load of β-FeOOH in the electrolyte was reduced to half. Despite the viscosity problem was improved, the Faradaic Efficiency did not increase significantly.
3. It is possible to efficiently deposit Fe directly from the residue (β-FeOOH based composition). The Fe electrodepositions based on the NR suspensions proved to be successful, not significantly less efficient when compared with the Fe_2O_3 suspensions results. The galvanostatic deposition at 90 ºC reached 59% Faradaic efficiency, mere ~2% above the Faradaic Efficiency of Fe_2O_3 suspensions in the same conditions.
4. The galvanostatic depositions from NR suspensions at higher temperatures with 18 M of NaOH showed, the Faradaic efficiency, in a general way, decreased as the temperature increases (apart from the deposition at 105 ºC and the potential increase), such as for the Fe_2O_3 suspensions, only to reach higher Faradaic efficiencies. At 120 ºC reached a maximum of 40% Faradaic efficiency and 21% at 130 ºC. At 105 ºC a 0.5% of Faradaic efficiency was obtained.
5. The potentiostatic depositions of NR suspensions showed high Faradaic efficiencies regardless the cathodic potentials applied in a range between -1.15 and -1.075 V. The Faradaic efficiencies at -1.075, -1.10 and -1.15 V potentials reached 91%, 82% and 83%, respectively.
6. All microstructures of the deposits showed the presence of Fe. The depositions from Fe_2O_3 and NR suspensions revealed homogeneous Fe deposits, in comparison with the synthetic β-FeOOH, with heterogeneous Fe deposits. Dendrites confirmed by XRD and EDS analysis.

4.1. Accomplishment of the objectives

The objectives outlined at the beginning of the thesis were accomplished.

- Synthesis and characterization of the composition of the NR.
- As a first approach, the production of Fe by electrochemical deposition in a NaOH alkaline suspension at low temperatures was evaluated. Following by the suspensions based on Fe_2O_3 and NR.
- Comparison of the electrochemical deposition of β-FeOOH-based suspensions with the NR. It was found that comparison is only possible at 90 ºC, due to the limitations of the synthetic material. Instead, the comparison was made with Fe_2O_3. For the following investigation, additional research on the β-FeOOH is necessary.
- The factors affecting Faradaic efficiencies, such as the temperature, the NaOH concentration and the β-FeOOH load on the solution and the material suspended in the solution were studied. The optimal conditions for the deposition were found.
- Studying mechanisms of electrodeposition.

4.2. Limitations and future work

The main limitation of the present work includes the short time imposed by the MSc Thesis work about studying more deeply all mechanisms of electroreduction for all the three suspensions. Thus, future work concerns improving the β-FeOOH synthesis and better understanding the behavior of the β -FeOOH-based suspensions.

Studies of the deposition conditions and their influence on the Faradaic efficiency of NR suspensions are also the aim of the future work. Modification of the residue, including acid and alkaline treatment, high-temperature annealing, and magnetic separation will be also studied.

References

[1] Worldsteel Association, “World Steel in Figures Report”, 2021, [Online]. Available: https://www.worldsteel.org/en/dam/jcr:976723ed-74b3-47b4-92f6-81b6a452b86e/World%2520Steel%2520in%2520Figures%25202021.pdf.

[2] L. Holappa, “Iron and Steel Technology”, *Treatise Process Metall.*, vol. 3, pp. 1–1, 2014, doi: 10.1016/B978-0-08-096988-6.00001-8.

[3] J. M. Cullen, J. M. Allwood, and M. D. Bambach, “Mapping the global flow of steel: From steelmaking to end-use goods”, *Environ. Sci. Technol.*, vol. 46, no. 24, pp. 13048–13055, 2012, doi: 10.1021/es302433p.

[4] E. R. Ramanaidou and M. A. Wells, *Sedimentary Hosted Iron Ores*, 2nd ed., vol. 13, no. March. Elsevier Ltd., 2013.

[5] V. Himanen, “Air quality”, *A Dict. Transp. Anal.*, pp. 15–18, 2010, doi: 10.1002/9780470057339.vaa013.

[6] S. Abouelfadl, “Global Warming – Causes, Effects and Solution’S Trials”, *JES. J. Eng. Sci.*, vol. 40, no. 4, pp. 1233–1254, 2012, doi: 10.21608/jesaun.2012.114490.

[7] COP26, “COP26 Explained”, *UN Clim. Chang. Conf. UK 2021*, 2021, [Online]. Available: https://ukcop26.org/.

[8] K. Xie and A. R. Kamali, “Electro-reduction of hematite using water as the redox mediator”, *Green Chem.*, vol. 21, no. 2, pp. 198–204, 2019, doi: 10.1039/c8gc02756k.

[9] S. Koutsoupa, S. Koutalidi, E. Bourbos, E. Balomenos, and D. Panias, “Electrolytic iron production from alkaline bauxite residue slurries at low temperatures carbon-free electrochemical process for the production of metallic iron”, *Johnson Matthey Technol. Rev.*, vol. 65, no. 3, pp. 366–374, 2021, doi: 10.1595/205651320x15918757312944.

[10] A. Allanore, H. Lavelaine, G. Valentin, J. P. Birat, and F. Lapicque, “Electrodeposition of Metal Iron from Dissolved Species in Alkaline Media”, *J. Electrochem. Soc.*, vol. 154, no. 12, p. E187, 2007, doi: 10.1149/1.2790285.

[11] A. Maihatchi, M. N. Pons, Q. Ricoux, F. Goettmann, and F. Lapicque, “Electrolytic iron production from alkaline suspensions of solid oxides: Compared cases of hematite, iron ore and iron-rich bayer process residues”, *J. Electrochem. Sci. Eng.*, vol. 10, no. 2, pp. 95–102, 2020, doi: 10.5599/jese.751.

[12] F. Trivinho-Strixino, J. S. Santos, and M. Souza Sikora, *Electrochemical Synthesis of Nanostructured Materials*. Elsevier Inc., 2017.

[13] E. C. S. Transactions and T. E. Society, “Electrodeposition of Iron in Aqueous Alkaline Solution: An Alternative to Carbothermic Reduction”, *Electrochem. Soc.*, vol. 16, no. 36, pp. 31–37, 2009, doi: 10.1149/1.3114006.

[14] Y. A. Ivanova *et al.*, “Electrochemical deposition of Fe and Fe/CNTs composites from strongly alkaline hematite suspensions”, *J. Appl. Electrochem.*, vol. 45, no. 5, pp. 515–522, 2015, doi: 10.1007/s10800-015-0803-6.

[15] M. Siebentritt, P. Volovitch, K. Ogle, and G. Lefèvre, “Adsorption and electroreduction of hematite particles on steel in strong alkaline media”, *Colloids Surfaces A Physicochem. Eng. Asp.*, vol. 440, pp. 197–201, 2014, doi:

10.1016/j.colsurfa.2012.09.002.

[16] A. Allanore, J. Feng, H. Lavelaine, and K. Ogle, “The Adsorption of Hematite Particles on Steel in Strongly Alkaline Electrolyte”, *J. Electrochem. Soc.*, vol. 157, no. 3, p. E24, 2010, doi: 10.1149/1.3273198.

[17] J. F. Monteiro, Y. A. Ivanova, A. V. Kovalevsky, D. K. Ivanou, and J. R. Frade, “Reduction of magnetite to metallic iron in strong alkaline medium”, *Electrochim. Acta*, vol. 193, pp. 284–292, 2016, doi: 10.1016/j.electacta.2016.02.058.

[18] V. Feynerol, H. Lavelaine, P. Marlier, M. N. Pons, and F. Lapicque, “Reactivity of suspended iron oxide particles in low temperature alkaline electrolysis”, *J. Appl. Electrochem.*, vol. 47, no. 12, pp. 1339–1350, 2017, doi: 10.1007/s10800-017-1127-5.

[19] M. Barberousse, A. Debregeas, M. Apostolou, and C. Bono, “Electrification of primary steel production based on ΣIDERWIN process: simulation on the European power system in 2050”, *"Proceedings “ ‘Industrial Effic. 2020’” Conf.*, pp. 435–443, 2020.

[20] A. Allanore, H. Lavelaine, J. P. Birat, G. Valentin, and F. Lapicque, “Experimental investigation of cell design for the electrolysis of iron oxide suspensions in alkaline electrolyte”, *J. Appl. Electrochem.*, vol. 40, no. 11, pp. 1957–1966, 2010, doi: 10.1007/s10800-010-0172-0.

[21] S. J. Lloyd, “S. J. Lloyd”, *Trans. Am. Electrochem. Soc.*, vol. 55, p. 305, 1929.

[22] J. A. M. LeDuc, R. E. Loftfield, and L. E. Vaaler, “Electrolytic Iron Powder from a Caustic Soda Solution”, *J. Electrochem. Soc.*, vol. 106, no. 8, p. 659, 1959, doi: 10.1149/1.2427467.

[23] S. Koutsoupa, S. Koutalidi, E. Balomenos, and D. Panias, “ΣIDERWIN—A New Route for Iron Production”, *Mater. Proc.*, vol. 5, no. 1, p. 58, 2021, doi: 10.3390/materproc2021005058.

[24] B. Yuan, O. E. Kongstein, and G. M. Haarberg, “Electrowinning of Iron in Aqueous Alkaline Solution Using a Rotating Cathode”, *J. Electrochem. Soc.*, vol. 156, no. 2, p. D64, 2009, doi: 10.1149/1.3039998.

[25] A. Maihatchi Ahamed, M. N. Pons, Q. Ricoux, F. Goettmann, and F. Lapicque, “Production of electrolytic iron from red mud in alkaline media”, *J. Environ. Manage.*, vol. 266, no. October 2019, 2020, doi: 10.1016/j.jenvman.2020.110547.

[26] D. V. Lopes, A. Kovalevsky, M. Quina, and J. Frade, “Electrochemical deposition of zero-valent iron from alkaline ceramic suspensions of Fe2-xAlxO3 for iron valorisation”, *J. Electrochem. Soc.*, pp. 2–10, 2020, doi: 10.1149/1945-7111/ab9a2b.

[27] ArcelorMittalMaizieres Research SA, “Siderwin”, *Siderwin website*, 2017. https://www.siderwin-spire.eu.

[28] K. E. Steve Healy, “Sustainable Bauxite Residue”, p. 92, 2022, [Online]. Available: www.international-aluminium.org.

[29] M. A. Khairul, J. Zanganeh, and B. Moghtaderi, “The composition, recycling and utilisation of Bayer red mud”, *Resour. Conserv. Recycl.*, vol. 141, no. November 2018, pp. 483–498, 2019, doi: 10.1016/j.resconrec.2018.11.006.

[30] K. Ishikawa, T. Yoshioka, T. Sato, and A. Okuwaki, “Solubility of hematite in LiOH, NaOH and KOH solutions”, *Hydrometallurgy*, vol. 45, no. 1–2, pp. 129–135, 1997, doi: 10.1016/s0304-386x(96)00068-0.

[31] X. Zou *et al.*, “Electroreduction of Iron(III) Oxide Pellets to Iron in Alkaline Media: A Typical Shrinking-Core Reaction Process”, *Metall. Mater. Trans. B Process Metall. Mater. Process. Sci.*, vol. 46, no. 3, pp. 1262–1274, 2015, doi: 10.1007/s11663-015-0336-8.

[32] M. Pourbaix, H. Zhang, and A. Pourbaix, “Presentation of an Atlas of chemical and electrochemical equilibria in the presence of a gaseous phase”, *Mater. Sci. Forum*, vol. 251–254, pp. 143–148, 1997, doi: 10.4028/www.scientific.net/msf.251-254.143.

[33] Y. A. Ivanova, J. F. Monteiro, L. B. Teixeira, N. Vitorino, A. V. Kovalevsky, and J. R. Frade, “Designed porous microstructures for electrochemical reduction of bulk hematite ceramics”, *Mater. Des.*, vol. 122, pp. 307–314, 2017, doi: 10.1016/j.matdes.2017.03.031.

[34] B. N. Ciribelli, F. Colmati, and E. C. de Souza, “Nernst equation applied to electrochemical systems and centenary of his Nobel Prize in chemistry”, *Int. J. Innov. Educ. Res.*, vol. 8, no. 11, pp. 670–683, 2020, doi: 10.31686/ijier.vol8.iss11.2803.

[35] D. V. Lopes, Y. A. Ivanova, A. V. Kovalevsky, A. R. Sarabando, J. R. Frade, and M. J. Quina, “Electrochemical reduction of hematite-based ceramics in alkaline medium: Challenges in electrode design”, *Electrochim. Acta*, vol. 327, p. 135060, 2019, doi: 10.1016/j.electacta.2019.135060.

[36] F. J. Morin, “Electrical properties of αfe2O3 and αfe2O3 containing titanium”, *Phys. Rev.*, vol. 83, no. 5, pp. 1005–1010, 1951, doi: 10.1103/PhysRev.83.1005.

[37] L. Vella and D. Emerson, “Electrical Properties of Magnetite- and Hematite-Rich Rocks and Ores”, *ASEG Ext. Abstr.*, vol. 2012, no. 1, pp. 1–4, 2012, doi: 10.1071/aseg2012ab232.

[38] D. V. Lopes *et al.*, “Alkaline Electrochemical Reduction of a Magnesium Ferrospinel into Metallic Iron for the Valorisation of Magnetite-Based Metallurgical Waste”, *J. Electrochem. Soc.*, vol. 168, no. 7, p. 073504, 2021, doi: 10.1149/1945-7111/ac1490.

[39] C. Tudisco, M. T. Cambria, and G. G. Condorelli, *Multifunctional Magnetic Nanoparticles for Theranostic Applications*. Elsevier Inc., 2018.

[40] K. R. Tolod, S. Hernández, E. A. Quadrelli, and N. Russo, “Visible Light-Driven Catalysts for Water Oxidation: Towards Solar Fuel Biorefineries”, *Stud. Surf. Sci. Catal.*, vol. 178, pp. 65–84, 2019, doi: 10.1016/B978-0-444-64127-4.00004-5.

[41] R. Chitrakar, S. Tezuka, A. Sonoda, K. Sakane, K. Ooi, and T. Hirotsu, “Phosphate adsorption on synthetic goethite and akaganeite”, *J. Colloid Interface Sci.*, vol. 298, no. 2, pp. 602–608, 2006, doi: 10.1016/j.jcis.2005.12.054.

[42] C. Rémazeilles and P. Refait, “On the formation of β-FeOOH (akaganéite) in chloride-containing environments”, *Corros. Sci.*, vol. 49, no. 2, pp. 844–857, 2007, doi: 10.1016/j.corsci.2006.06.003.

[43] T. S. Peretyazhko *et al.*, “Synthesis of akaganeite in the presence of sulfate: Implications for akaganeite formation in Yellowknife Bay, Gale Crater, Mars”,

Geochim. Cosmochim. Acta, vol. 188, pp. 284–296, 2016, doi: 10.1016/j.gca.2016.06.002.

[44] H. Morimoto, K. Takeno, Y. Uozumi, K. I. Sugimoto, and S. I. Tobishima, "Synthesis of composite electrode materials of FeOOH-based particles/carbon powder and their high-rate charge-discharge performance in lithium cells", *J. Power Sources*, vol. 196, no. 15, pp. 6512–6516, 2011, doi: 10.1016/j.jpowsour.2011.03.033.

[45] J. Cai, J. Liu, Z. Gao, A. Navrotsky, and S. L. Suib, "Synthesis and anion exchange of tunnel structure akaganeite", *Chem. Mater.*, vol. 13, no. 12, pp. 4595–4602, 2001, doi: 10.1021/cm010310w.

[46] R. M. Cornell and U. Schwertmann, "Chapter 19: Applications", *Iron Oxides Struct. Prop. React. Occur. Uses*, pp. 509–524, 2003.

[47] J. Zhao, W. Lin, Q. Chang, W. Li, and Y. Lai, "Adsorptive characteristics of akaganeite and its environmental applications: a review", *Environ. Technol. Rev.*, vol. 1, no. 1, pp. 114–126, 2012, doi: 10.1080/09593330.2012.701239.

[48] K. Ståhl *et al.*, "On the akaganéite crystal structure, phase transformations and possible role in post-excavational corrosion of iron artifacts", *Corros. Sci.*, vol. 45, no. 11, pp. 2563–2575, 2003, doi: 10.1016/S0010-938X(03)00078-7.

[49] E. A. Deliyanni, D. N. Bakoyannakis, A. I. Zouboulis, K. A. Matis, and L. Nalbandian, "Akaganéite-type β-FeO(OH) nanocrystals: Preparation and characterization", *Microporous and Mesoporous Materials*, vol. 42, no. 1. pp. 49–57, 2001, doi: 10.1016/S1387-1811(00)00259-6.

[50] D. N. Bakoyannakis, E. A. Deliyanni, A. I. Zouboulis, K. A. Matis, L. Nalbandian, and T. Kehagias, "Akaganeite and goethite-type nanocrystals: Synthesis and characterization", *Microporous Mesoporous Mater.*, vol. 59, no. 1, pp. 35–42, 2003, doi: 10.1016/S1387-1811(03)00274-9.

[51] M. Nesterova, J. Moreau, and J. F. Banfield, "Model biomimetic studies of templated growth and assembly of nanocrystalline FeOOH", *Geochim. Cosmochim. Acta*, vol. 67, no. 6, pp. 1185–1195, 2003, doi: 10.1016/s0016-7037(02)01180-8.

[52] T. Sugimoto, S. Waki, and A. Muramatsu, "Preparation of monodisperse platelet-type hematite particles from a highly condensed /3-FeOOH suspension", *Colloids Surfaces A Physicochem. Eng. Asp.*, vol. 109, pp. 155–165, 1996, [Online]. Available: https://doi.org/10.1016/0927-7757(95)03454-4.

[53] M. Žic, M. Ristić, and S. Musić, "Effect of phosphate on the morphology and size of α-Fe2O3 particles crystallized from dense β-FeOOH suspensions", *J. Alloys Compd.*, vol. 466, no. 1–2, pp. 498–506, 2008, doi: 10.1016/j.jallcom.2007.11.075.

[54] M. Žic, M. Ristić, and S. Musić, "The effect of temperature on the crystallization of α-Fe2O3 particles from dense β-FeOOH suspensions", *Mater. Chem. Phys.*, vol. 120, no. 1, pp. 160–166, 2010, doi: 10.1016/j.matchemphys.2009.10.040.

[55] A. Abdullah and A. Mohammed, "Scanning Electron Microscopy (SEM): A Review Scanning Electron Microscopy (SEM): A Review", *Proc. 2018 Int. Conf. Hydraul. Pneum. - HERVEX*, no. January, pp. 77–85, 2019.

[56] J. Tedim, "Interacções entre o Feixe de Electrões e a Matéria", pp. 1–9, 2018.

[57] W. Zhou, R. Apkarian, Z. L. Wang, and D. Joy, “Fundamentals of scanning electron microscopy (SEM)”, *Scanning Microsc. Nanotechnol. Tech. Appl.*, pp. 1–40, 2007, doi: 10.1007/978-0-387-39620-0_1.

[58] M. Almeida, “Difracção de raios X Ano Lectivo 2015-2016 A Difracção de Raios X no Estudo dos Materiais”, pp. 1–22, 2016.

[59] J. Stangl, C. Mocuta, V. Chamard, and D. Carbone, “X-Ray Diffraction Principles”, *Nanobeam X-Ray Scatt.*, no. 1913, pp. 13–38, 2013, doi: 10.1002/9783527655069.ch2.

[60] J. Stangl, C. Mocuta, V. Chamard, and D. Carbone, *Nanobeam X-Ray Scattering Probing Matter at the Nanoscale*. 2014.

[61] T. Report, *Application of a Portable X-Ray Fluorescence Technique to Assess Concrete Mix Proportions*, vol. 00011, no. March. 2012.

[62] S. J. Blott, D. J. Croft, K. Pye, S. E. Saye, and H. E. Wilson, “Particle size analysis by laser diffraction”, *Geol. Soc. Spec. Publ.*, vol. 232, pp. 63–73, 2004, doi: 10.1144/GSL.SP.2004.232.01.08.

[63] Metrohm, “Metrohm – Autolab”, 2013. [Online]. Available: https://www.metrohm-autolab.com/download/Autolab_Brochure_2013_EN_LR.pdf.

[64] D. V. Lopes, A. D. Lisenkov, L. C. M. Ruivo, A. A. Yaremchenko, J. R. Frade, and A. V. Kovalevsky, “Prospects of Using Pseudobrookite as an Iron-Bearing Mineral for the Alkaline Electrolytic Production of Iron”, *Materials (Basel).*, vol. 15, no. 4, pp. 1–19, 2022, doi: 10.3390/ma15041440.

Attachment

Table 6: Deposited mass (g) on the cathode and Faradaic efficiency (%) achieved from NR, β-FeOOH and Fe_2O_3 suspensions at 90ºC.

Material	Load	Deposited mass (g)	Efficiency (%)
NR	100 g/L	0.165	59.3
β-FeOOH	50 g/L	0.004	6.2
β-FeOOH	100 g/L	0.003	4.32
Fe_2O_3	100 g/L	0.158	56.96

Table 7: Deposited mass (g) on the cathode and Fardaic efficiency (%) achieved from NR (orange) and Fe_2O_3 (green) suspensions at 105, 120 and 130 ºC.

Temperature (ºC)	Deposited mass (g)	Efficiency (%)
105	0.0014	0.504
	0.233	83.8
120	0.111	39.8
	0.191	68.9
130	0.058	21.0
	0.133	48.1